

Geochemistry, Geophysics, Geosystems



RESEARCH ARTICLE

10.1029/2021GC009803

Key Points:

- In 2019 Taupō volcano underwent a period of volcanic unrest, indicated by multiple seismic swarms and ground deformation
- Earthquakes define a brittle-ductile transition around an aseismic zone that is coincident with an inflating deformation source
- These observations suggest the presence of ≥ 250 km³ of magma mush in the mid-crust with >20%–30% melt fraction

Supporting Information:

Supporting Information may be found in the online version of this article.

Correspondence to:

F. Illsley-Kemp,
finnigan.illsleykemp@vuw.ac.nz

Citation:

Illsley-Kemp, F., Barker, S. J., Wilson, C. J. N., Chamberlain, C. J., Hreinsdóttir, S., Ellis, S., et al. (2021). Volcanic unrest at Taupō volcano in 2019: Causes, mechanisms and implications. *Geochemistry, Geophysics, Geosystems*, 22, e2021GC009803. <https://doi.org/10.1029/2021GC009803>

Received 19 MAR 2021

Accepted 1 JUN 2021

Volcanic Unrest at Taupō Volcano in 2019: Causes, Mechanisms and Implications

Finnigan Illsley-Kemp¹ , Simon J. Barker¹ , Colin J. N. Wilson¹ , Calum J. Chamberlain¹ , Sigrún Hreinsdóttir² , Susan Ellis² , Ian J. Hamling² , Martha K. Savage¹ , Eleanor R. H. Mestel¹ , and Fabian B. Wadsworth³ 

¹School of Geography, Environment and Earth Sciences, Victoria University of Wellington, Wellington, New Zealand, ²GNS Science, Lower Hutt, New Zealand, ³Department of Earth Sciences, Durham University, Durham, UK

Abstract Taupō volcano, New Zealand, is a large caldera volcano that has been highly active through the Holocene. It most recently erupted ~1,800 years ago but there have been multiple periods of historic volcanic unrest. We use seismological and geodetic analysis to show that in 2019 Taupō underwent a period of unrest characterized by increased seismic activity through multiple swarms and was accompanied by ground deformation within the caldera. The earthquakes, which include non-double-couple events, serve to outline an aseismic zone beneath the most recent eruptive vents. This aseismic zone is coincident with an inflating source, based on forward modeling of ground deformation data. We infer that this aseismic and deforming region delineates the location of the present day magma reservoir that is ≥ 250 km³ in volume and has a melt fraction of >20%–30%, inhibiting seismic activity. Our analysis shows that the 2019 unrest at Taupō was volcanic in nature and origin, demonstrating that this is an active and potentially hazardous volcano, and that improving our monitoring and understanding of its behavior is important.

Plain Language Summary Taupō in New Zealand, is a large caldera volcano which has been very active in recent geological time, but has not erupted for about 1,800 years. However, in historical times it has undergone periods of unrest involving abundant, sometimes damaging earthquakes, and ground deformation, but no eruption. In 2019, Taupō volcano underwent one of these unrest periods, represented by a large increase in the number of earthquakes and observable ground deformation within the caldera. Using the locations and patterns of the earthquakes and ground deformation allow us to infer that beneath the caldera there is an active magma reservoir of at least 250 km³ volume and which is at least 20%–30% molten. New magma being fed into this reservoir caused the triggering of earthquakes in the surrounding brittle crust along fault lines that reflect both the volcano structure and the regional rift faults that cut across the volcano. Our findings show that Taupō needs to be carefully monitored to better understand the processes at depth and the factors that might cause similar unrest to escalate into an eruption in the future.

1. Introduction

One of the fundamental goals of modern volcanology is the accurate and timely forecasting of impending eruptions in order to mitigate the risk to the affected populations and infrastructure (e.g., Goitom et al., 2015; Mei et al., 2013; Syahbana et al., 2019). Although modern monitoring techniques can provide detailed insights into the inner magmatic workings of volcanoes, the inherent complexity of volcanic systems means that precise forecasting of eruptions is usually not achievable (Sparks, 2003), especially when volcanoes are demonstrably capable of unprecedented or unique events (Wilson, 2017). Periods of activity where there is a detectable deviation in geophysical (e.g., seismicity, ground deformation) or geochemical (e.g., fluid emissions) signals from a long-term baseline to an elevated state are labeled as “unrest” (Phillipson et al., 2013). Most volcanic eruptions are preceded by variable levels of unrest that range in severity and timing from volcano to volcano and usually last anywhere from a few hours to several years (Acocella et al., 2015). However, significant unrest episodes often occur without leading to eruption (e.g., Newhall & Dzurisin, 1988). This asymmetric relationship between unrest and eruption (i.e., eruptions are always preceded by unrest, but unrest is not always followed by eruption) highlights the challenges with the nonlinear nature of volcanic

© 2021. The Authors.

This is an open access article under the terms of the [Creative Commons Attribution-NonCommercial-NoDerivs License](https://creativecommons.org/licenses/by-nc-nd/4.0/), which permits use and distribution in any medium, provided the original work is properly cited, the use is non-commercial and no modifications or adaptations are made.

systems, the importance of volcano monitoring (Sparks, 2003), and the need to be able to interpret subsurface processes on suitable timescales for adequate warning and advice.

Detecting volcanic unrest signals is particularly important at silicic caldera volcanoes, which have produced Earth's largest explosive eruptions (e.g., Christiansen, 2001; Lavigne et al., 2013; Mason et al., 2004; Rose & Chesner, 1987; Takarada & Hoshizumi, 2020) with potentially devastating impacts on local, regional, and even global scales (Robock, 2000; Self, 2006). Rhyolitic caldera volcanoes are perceived to be amongst the most dangerous volcanoes and have gained much research attention from scientists and general intrigue from the public (Johnston et al., 2002; Lowenstern et al., 2006; Troise et al., 2007). Caldera-forming eruptions are high-impact, low frequency events with widespread hazards (Papale, 2018) and it is generally assumed that such large magnitude eruptions would be preceded by significant unrest (Acocella et al., 2015). However, caldera volcanoes are also associated with smaller, more frequent eruptions and can display a wide range of eruption styles within explosive to effusive regimes (e.g., Christiansen, 2001; Nairn, 2002; Newhall & Dzurisin, 1988; Wilson, 1993). Forecasting the future behavior of caldera volcanoes can be challenging with many possible scenarios of unrest or eruption with widely ranging associated hazard types and impacts (Charlton et al., 2020; Christiansen et al., 2007; Hildreth, 2017; Hill et al., 2020). This challenge is rendered more complex because a high proportion of caldera volcanoes are set within areas that have extensional tectonic regimes in the shallow crust (Hughes & Mahood, 2011), and so there is scope for tectonic processes to contribute to seismic activity and generate unrest in the geographic area of the volcano, but which is not volcanic unrest as such.

As with other types of volcano, unrest at caldera volcanoes typically manifests as earthquake swarms, ground deformation, changes to the local gravity and magnetic fields, and changes to fluid discharge volumes, temperatures, and chemistries (Acocella et al., 2015; Newhall & Dzurisin, 1988; Sandri et al., 2004; 2017). However, interpreting caldera unrest is further complicated by several inescapable factors. First, caldera volcanoes are associated with large, long-lived and geometrically complex magmatic systems (e.g., Acocella et al., 2015; Bachmann & Huber, 2016). Magmatic processes can be difficult to interpret due to the vertically extensive and compositionally heterogeneous nature of the broader magmatic reservoir and its potentially limited surface expression (e.g., Ellis et al., 2007, in the present context). Second, monitoring is often complicated by the presence of one or more highly active, shallower hydrothermal system(s) that can generate their own unrest signals in the form of enhanced seismicity, uplift, and fluid chemistry/fluxes reflecting processes such as enhanced boiling (e.g., Chiarabba & Moretti, 2006; Hildreth, 2017; Hill et al., 2020; Hutchison et al., 2016). These signals can be entirely non-magmatic and reflect pressure variations from changing permeability and fracture networks resulting from mineral dissolution/precipitation or even stress changes from regional earthquakes (e.g., Acocella et al., 2015; Husen et al., 2004; Troise et al., 2019). Third, caldera volcanoes cover a large geographical footprint (typically hundreds of square kilometers) with widely distributed vents, numerous hydrothermal features, and tectonic structures (e.g., basins, faults). Fault slip within or outside the caldera can occur due to local tectonic processes and may have little or nothing to do with changes in the magmatic system, although changes in regional stress field may in-turn directly impact the magmatic or hydrothermal system(s) (Hill et al., 2002). Fourth, as calderas are large depressions they are often infilled by large lakes, making monitoring logistically challenging (e.g., Illsley-Kemp et al., 2020; Singer et al., 2014). Ultimately, a wide range of processes can trigger unrest at calderas and it can be challenging to disentangle the multiple underlying causes (Acocella et al., 2015) and decide if the unrest presages an eruption (Hincks et al., 2014).

The great majority of caldera unrest episodes documented globally do not lead to an eruption, despite potentially dramatic variations in monitoring parameters (e.g., up to meters of ground deformation, coupled with severe seismicity: Chang et al., 2007; Hill, 2006; Tizzani et al., 2009; Troise et al., 2019; Peterson et al., 2020). Due to the reputation of caldera volcanoes as a source of devastating eruptions, however, non-eruptive unrest episodes themselves can cause significant socio-economic impacts through uncertainty around possible future activity and triggering of precautionary mitigation efforts (e.g., Barberi et al., 1984; Johnston et al., 2002; Longo, 2019; Maj et al., 1989; Potter, Scott, Jolly, Johnston, & Neall, 2015). Therefore, improving our understanding of the processes that drive volcanic unrest at calderas is not only an important step toward forecasting whether an eruption is likely or imminent (Acocella et al., 2015) but also can greatly strengthen public awareness through scientific communication (Charlton et al., 2020). Here we investigate

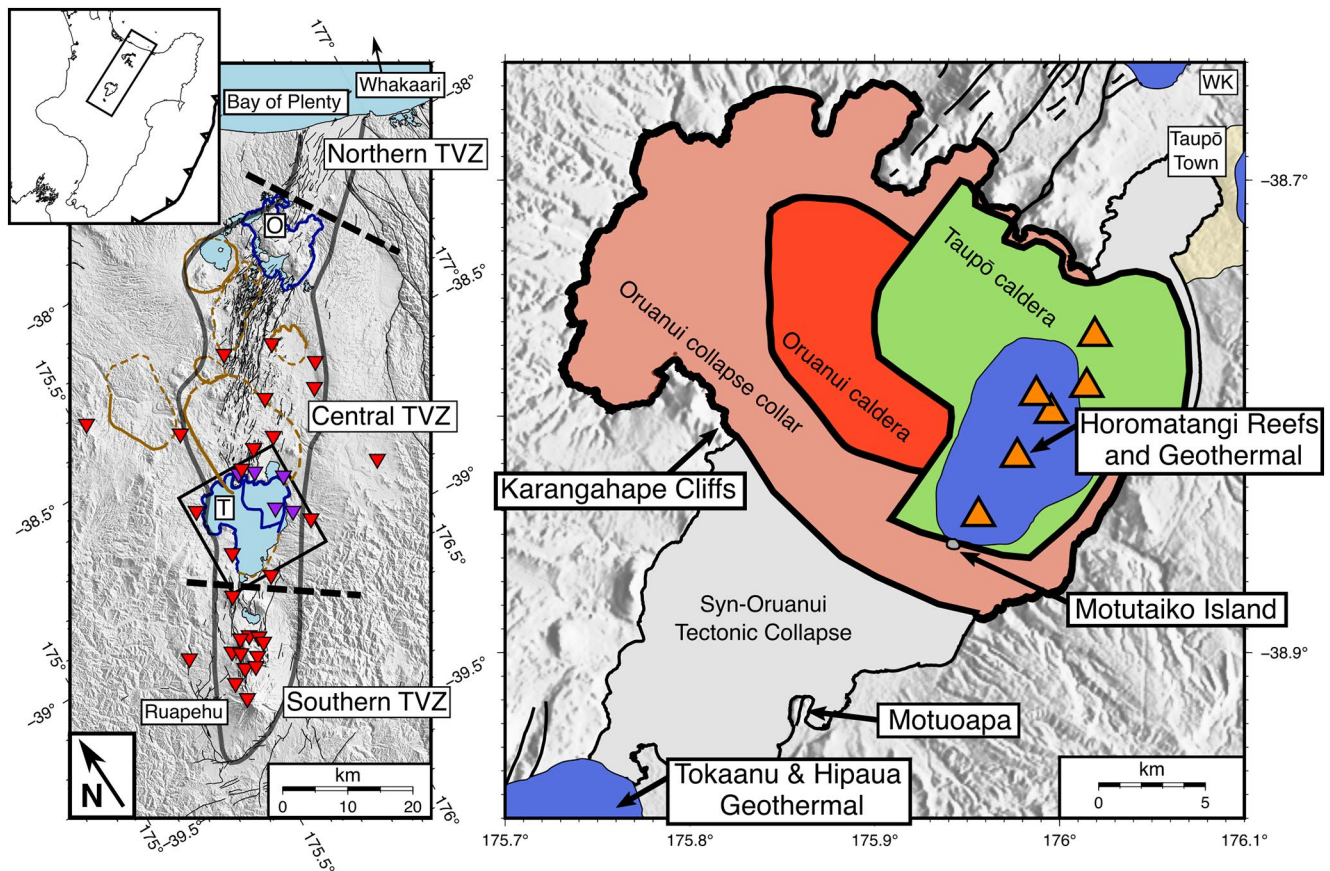


Figure 1. Left: The Taupō Volcanic Zone (TVZ) in New Zealand's North Island. The gray line marks the boundaries of the young TVZ (envelope around vents active in the last 350 kyr), which is divided into the southern, central, and northern sections along its length. The southern and northern TVZ are characterized by andesite volcanism, whereas the central TVZ is dominated by caldera-related rhyolitic volcanism (Wilson et al., 1995, 2009). Dark blue outlines denote the currently active calderas, Taupō in the south, and Okataina in the north, brown outlines denote older calderas. The mapped active faults are shown in black (Langridge et al., 2016, <http://data.gns.cri.nz/af/>). Red and purple inverted triangles show the locations of the seismometers and GNSS sites, respectively, from which the data were used in this study. Right: Major features of Taupō volcano. The red regions denotes the Oruanui eruption collapse caldera and collar (25.5 ka) (Wilson, 2001), the green region denotes the Taupō eruption collapse caldera (232 CE) (Davy & Caldwell, 1998; Hogg et al., 2012). The orange triangles denote vent locations from the last 2.15 ka (Barker et al., 2015) and the nearby blue region denotes the Horomatangi Reefs and active geothermal system (de Ronde et al., 2002). WK denotes the location of the Wairakei geothermal power station.

a recent period of volcanic unrest at Taupō volcano in New Zealand's North Island (Figure 1). Taupō was the site of the youngest known supereruption on Earth at 25.5 ka and also one of the most violent eruptions in the past 5,000 years at 232 ± 10 CE (Dunbar et al., 2017; Hogg et al., 2012; Wilson, 2001; Wilson & Walker, 1985). The magmatic system beneath Taupō remains active, as demonstrated by the ~ 120 MW thermal discharge near the site of the youngest vents (de Ronde et al., 2002) and is considered capable of producing future explosive eruptions (Barker et al., 2015, 2016, 2021). In 2019, Taupō experienced a series of earthquake swarms, which featured the largest earthquake within the caldera since 1952 (Ilsley-Kemp et al., 2020). In this study, we assess the timing and nature of Taupō's seismicity during 2019 to interpret the underlying causes of unrest, with implications for the state of the current magmatic system and the processes occurring under one of the largest and most hazardous caldera volcanoes on Earth.

2. Geological Background

2.1. Taupō Volcano

Taupō is a large silicic caldera volcano that lies within the Taupō Volcanic Zone (TVZ) in New Zealand's North Island (Te Ika-a-Māui) (Barker et al., 2021; Figure 1). The TVZ can be subdivided into three segments along its length. The southern and northern segments are characterized by andesite volcanism (e.g.,

Ruapehu and Whakaari/White Island), while the central segment is dominated by rhyolite and contains numerous caldera volcanoes that collectively make up the most productive region of Quaternary silicic volcanism on Earth (Wilson et al., 1995, 2009). The two currently active caldera volcanoes are Taupō and Okataina, situated at the southern and northern ends of the central TVZ, respectively (Figure 1). Taupō and Okataina have erupted a combined volume of $>770 \text{ km}^3$ of overwhelmingly rhyolitic magma over the last ~ 60 kyr (Wilson et al., 2009). Volcanism in the TVZ is ultimately driven by the subduction of the Hikurangi plateau (Pacific plate) beneath the North Island (Australian plate) and the hyperactive volcanism at Taupō and Okataina is fueled by subcrustal basaltic magmas originating from high degrees of partial melting in the mantle wedge (Barker et al., 2020; Eberhart-Phillips et al., 2020). The TVZ is also coincident with the Taupō continental rift (Figure 1), which has present day extension rates increasing from ≤ 5 mm/yr at Ruapehu in the south to 13–19 mm/yr at the Bay of Plenty in the north (Lamarche et al., 2006; Villamor et al., 2017; Wallace et al., 2004).

Taupō volcano is largely occupied by Lake Taupō, which infills the caldera collapse structure and obscures most of the young vent sites (Barker et al., 2021). The structural caldera is clearly defined by the largest negative gravity anomaly in the central North Island (Davy & Caldwell, 1998; Stagpoole et al., 2020) and was primarily formed by the structural collapse associated with the 25.5 ka Oruanui supereruption (Wilson, 2001). The southern section of the lake does not coincide with a negative gravity anomaly but is also thought to have partially collapsed during the Oruanui eruption (Wilson, 2001; Figure 1). The twenty-eight post-Oruanui eruptions (25 during the last 12 ka) range greatly in size and eruption style, with the latest and largest explosive event occurring at 232 ± 10 CE (Barker et al., 2015, 2019; Hogg et al., 2012, 2019; Wilson, 1993). This 232 CE “Taupō eruption” occurred in the northeast corner of the Oruanui caldera and caused further collapse (Davy & Caldwell, 1998, Figure 1). The Taupō eruption incorporated seven distinct explosive phases defined by changes in eruption style, intensity, degrees of magma-water interaction, and vent position (Healy, 1964; Houghton et al., 2010, 2014; Froggatt, 1981; Smith, 1998; Smith & Houghton, 1995; Wilson & Walker, 1985). The explosive eruption sequence climaxed with the opening of a rift-aligned fissure, which generated a pyroclastic density current that traveled radially outward at more than 200–300 m/s and devastated a $\sim 20,000 \text{ km}^2$ area (Wilson, 1985). About 10–20 years after this explosive activity a subaqueous dome-forming eruption occurred (Barker et al., 2016; Von Lichten et al., 2016; Wilson, 1993) and this formed the modern-day Horomatangi Reefs and Waitahanui Bank (Figure 1), the first of which is closely associated with active hydrothermal venting and high heat flow (de Ronde et al., 2002, Whiteford, 1996).

Our understanding of the location, depth, size, and state of the present-day magma reservoir at Taupō is hampered by the limited geophysical data over the area occupied by Lake Taupō (Barker et al., 2021). However, the temporal connection of post-Oruanui magma compositions highlight that a substantial silicic magma system has rebuilt and can produce eruptible silicic melt bodies on timescales of human interest and concern (Barker et al., 2015, 2016; Sutton et al., 2000). Based on Holocene vent positions and magma storage depths from petrological estimates, a first order estimate is that between 200 and $1,000 \text{ km}^3$ of crystal mush likely exists at 5–8 km depth beneath the modern Lake Taupō (Barker et al., 2015, 2021). Seismic imaging to the north of Taupō suggests that the quartzofeldspathic crust is only ~ 15 –16 km thick and is underlain by a region of mafic underplating that ultimately provides the heat and material to the shallower silicic system (Harrison & White, 2006; Stern et al., 2010; Stern & Benson, 2011; Stratford & Stern, 2006). Seismic anisotropy studies also suggests that a sizable magma reservoir is present beneath Taupō (Illsley-Kemp et al., 2019), but the presence of New Zealand’s largest lake means there has been no direct geophysical imaging of the magma reservoir and this is a key goal of future research (Barker et al., 2021; Illsley-Kemp et al., 2020).

2.2. Historic Unrest at Taupō

Determining whether a volcano is in a state of unrest can be an important step for forecasting eruption scenarios and informing end-users in charge of decision making and mitigation (e.g., the general populace, civil defense, and governments) (Charlton et al., 2020). Potter, Scott, Jolly, Johnston, and Neall (2015) developed a catalog of volcanic unrest at Taupō spanning 1872–2011 and suggested that there had been 16 unrest episodes (4 moderate, 12 minor) during that time period. Using a “Volcanic Unrest Index” (VUI: Potter, Scott, Jolly, Neall, & Johnston, 2015) they defined moderate unrest at Taupō as having the following

characteristics: earthquake swarms lasting between 90 days and 6 months, earthquakes occurring between 4 and 8 km depth within the caldera, more than 30 magnitude >4 earthquakes per month, and/or a ground deformation rate of more than 100 mm/year from a source at 4–8 km depth. Potter, Scott, Jolly, Johnston, and Neall (2015) suggested that there were periods of moderate volcanic unrest in 1887, 1922–1923, 1964–1965, and 1983–1984. However, prior to 1985 the seismograph network in New Zealand was sparse, particularly in the Taupō area, making it difficult to accurately locate earthquakes and to confidently assess whether these periods of activity were specifically related to the activity at the volcano (Barker et al., 2021). While the use of the VUI system at Taupō aids in rapid assessment to assist end-users, further complications arise because Taupō volcano is traversed by many rift related faults, and there are several large hydrothermal systems in and around the volcano (Figure 1). Thus, periods of unrest in the broader Taupō region may have little or nothing to do with changes in the volcano itself. Monitoring at Taupō is presently undertaken by the use of seismometers and GNSS sensors around the lake (Figure 1), allowing modern unrest episodes to be assessed in greater detail. In 2019, the National Geohazard Monitoring Network (GeoNet) detected 715 earthquakes ($M > 0.8$) in the Taupō region, approximately two times more than in a typical year. We use the publicly available data from the monitoring network provided by GeoNet (Petersen et al., 2011) to investigate this distinct period of heightened seismic activity.

3. Data and Methods

We downloaded earthquake arrival time (pick) information from GeoNet (Petersen et al., 2011) for all earthquakes that were detected in the Taupō region (area shown in Figure 3) in 2019 (715 earthquakes). Each earthquake was manually inspected and picks were adjusted/added accordingly for the 29 regional GeoNet seismometers (9 broad-band, 20 short-period). To increase the size of the earthquake template catalog (see details later) we also manually picked phases for GeoNet-detected earthquake from the Taupō area between 2010 and 2018 (1712 earthquakes). These earthquakes were then located using NonLinLoc's oct-tree sampling algorithm (Lomax et al., 2000). We use a 1D velocity model based on a seismic-refraction study from the area (Figure S11; Stern & Benson, 2011), this more accurately represents the local crustal structure than nationwide velocity models (e.g., Eberhart-Phillips et al., 2010). These earthquakes were then used to generate templates to detect additional earthquake detections from the continuous data using the matched-filter package EQcorrscan (Chamberlain et al., 2018).

Template waveforms were cut from the daylong data and filtered between 2 and 15 Hz using a fourth-order Butterworth band-pass filter. We cut templates to 4 s length starting 0.4 s before the P and S picks on the vertical and horizontal channels respectively. Template waveforms were then correlated with the continuous data between January 01, 2010 and December 31, 2019 processed in the same way as the templates. Daylong normalized correlations were time-shifted to align with template move outs and summed to generate daylong cross-correlation sums. Detections were made when the summed daylong correlations exceeded $0.4 \times$ the number of channels. To avoid duplicate detections for individual templates arising from cycle skipping, if multiple detections for an individual template occurred within 1 s of another detection we retained only the highest correlated detection. For each detection, we then computed cross-correlation derived phase-picks following the method outlined in Warren-Smith et al. (2017). We allowed a shift of up to 0.5 s and only retained picks with normalized correlations of at-least 0.4, and events with picks on a minimum of four stations. This analysis resulted in a total of 7314 earthquake detections in 2019, which we located with NonLinLoc (Lomax et al., 2000) and the same velocity model used to locate the template events. Some detections with a small number of phases are poorly located and cluster along vertical boundaries in the location grid, but these are not used in the later relocation. Each earthquake was assigned a unique ID number, based on the GeoNet format. If an earthquake in the catalog was also in the GeoNet catalog, we used the GeoNet assigned ID (e.g., 2019p665658), if the event was detected and picked by the EQcorrscan procedure the ID has a “d” flag (e.g., 2019d005968), finally if the event was not recorded by GeoNet but was manually picked and used as a template it has an “m” flag (e.g., 2019m000056).

We then generated differential pick times based on waveform correlation on a 2 s window around each pick, 0.5 s before the pick, allowing the pick to adjust by up to 0.3 s. We computed differential pick-times for all event pairs (not just template-detection pairs) within a maximum hypocentral separation of 8 km. These differential pick times were then used to relocate the entire catalog using the double-difference relocation

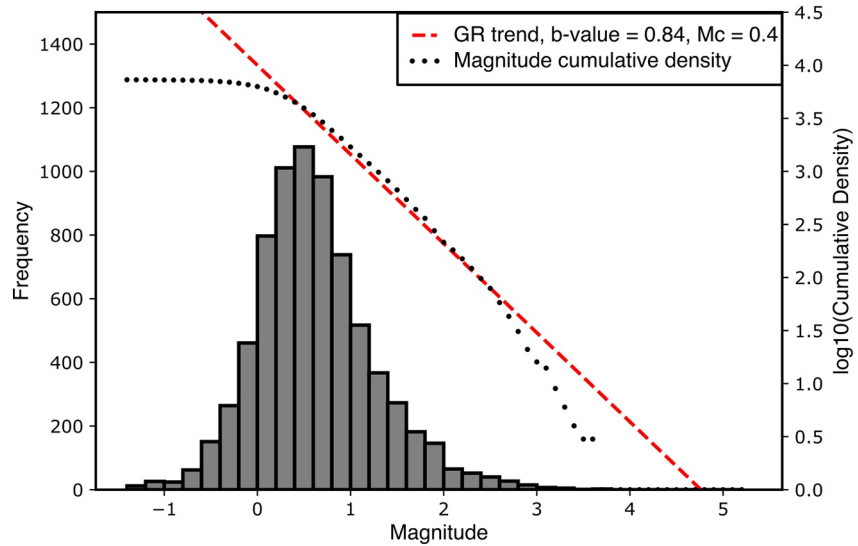


Figure 2. Magnitude-frequency distribution for Taupō seismicity in 2019. The earthquake catalog consists of 7314 earthquakes ranging from M_L -1.7 to 5.3 with a magnitude of completeness (M_c) of 0.4 and a b -value of 0.84 (see text for the procedure for deriving this catalog).

program GrowClust (Trugman & Shearer, 2017), requiring a minimum correlation of 0.6 and maximum cluster shifts of 2 km. Using this threshold we were able to relocate a total of 2432 earthquakes, which we use for our detailed analysis here. The mean NonLinLoc derived absolute 68% confidence ellipsoid, representing location errors for the subsequently relocated earthquakes, is ± 1.56 km and ± 2.15 km for the horizontal and vertical directions, respectively. The relative location errors derived from the internal GrowClust bootstrapping analysis for the relocated earthquakes are ± 1.01 km and ± 0.78 km for the horizontal and vertical directions, respectively. We also calculate average location errors for each discussed earthquake swarm, these are detailed in the Results section and are similar to the average for the overall catalog. This means that we can interpret the internal shape and structure of the earthquake clusters, and their positions relative to one another, with a high level of confidence whereas slightly more caution is required when interpreting absolute locations and depths.

In order to calculate accurate local magnitudes (M_L) for the catalog we first convolved the seismograms for each earthquake with the Wood-Anderson standard response (Anderson & Wood, 1925; Richter, 1935) and measured the peak-to-trough displacement amplitude on the vertical component. We then use these measurements to directly invert for a local-magnitude scale following the method of Keir et al. (2006) and Illsley-Kemp et al. (2017). This results in the following equation:

$$M_L = \log(A) - \log(A_0) + C, \quad (1)$$

where A is the Wood-Anderson displacement (in mm), C is an empirical station correction for each component of each seismometer, and $-\log(A_0)$ is a displacement correction term using a 17 km normalization (Hutton & Boore, 1987) such that:

$$-\log(A_0) = 1.5337 \log(r / 17) + 0.002343(r - 17) + 2, \quad (2)$$

where r is the hypocentral distance (km) and the constants, related to geometrical spreading and attenuation, have been directly solved and are specific to the Taupō region. The resulting magnitudes for the catalog range from -1.7 to 5.3 . We use the maximum curvature method (Wiemer & Wyss, 2000) to estimate a magnitude of completeness of 0.4 and a b -value of 0.84 (Figure 2).

To calculate moment tensor solutions we used manually determined P-wave polarities as an input to the Bayesian moment tensor source inversion software MTfit (Pugh & White, 2018). For each chosen event, we run both a double-couple constrained and full moment tensor inversion. If the polarities can be explained by a double-couple solution, we assume that it is and use the Bayesian derived highest probability solution.

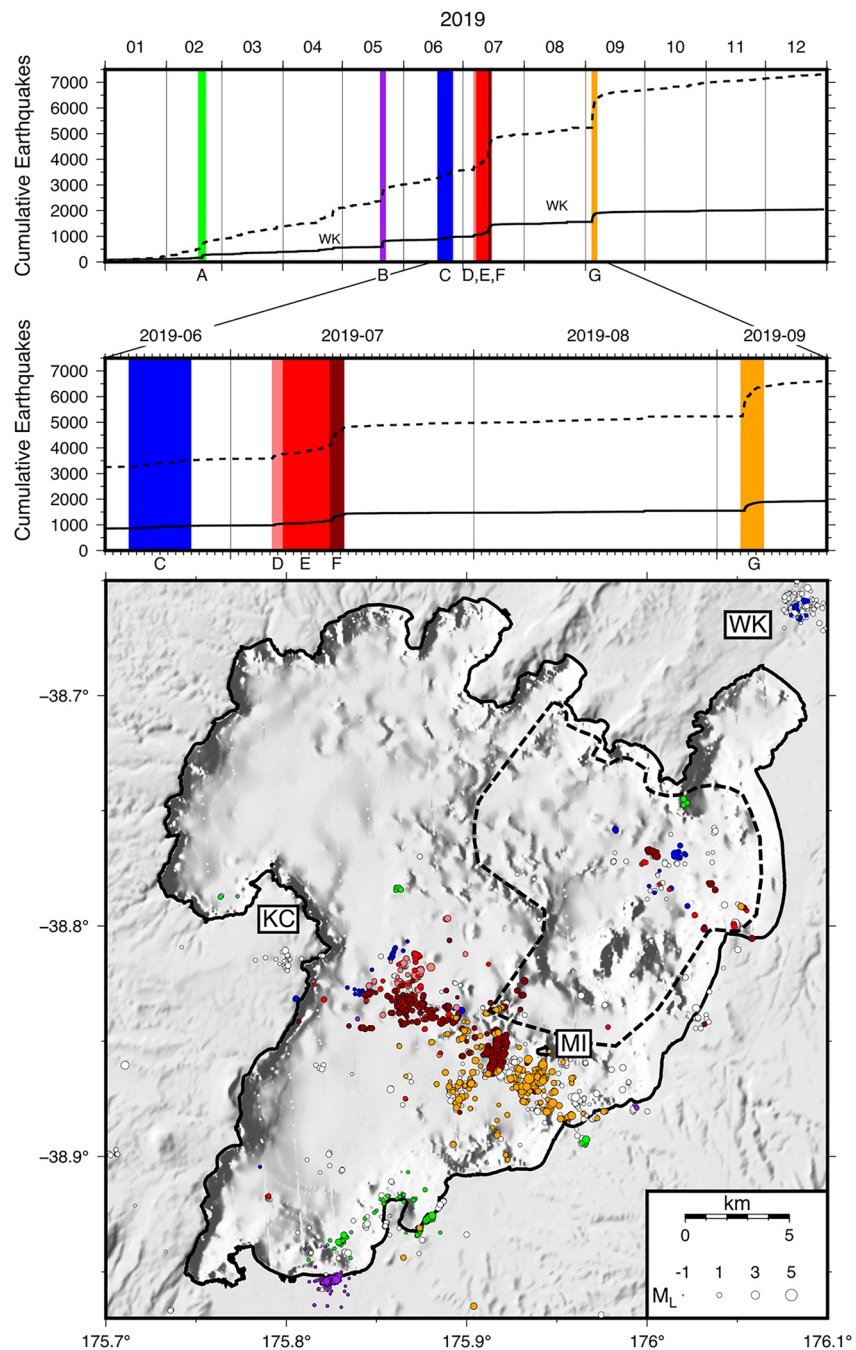


Figure 3. Map of the Lake Taupō area showing the locations of the 2019 earthquake swarms, colored by swarm. White filled circles represent earthquakes that are not assigned to a specific swarm. Only earthquakes that are relocated by GrowClust are shown (see text), and they are scaled by magnitude. KC, Karangahape Cliffs; MI, Motutaiko Island; WK, Wairakei geothermal plant. The top panel shows the cumulative number of earthquakes through time both for the entire catalog (dashed line) and the relocated catalog (solid line). Colored time-periods correspond to individual swarms A–G described in the text. Time periods labeled “WK” and labeled on the map denote periods of the increased earthquake activity at the Wairakei-Tauhara geothermal system.

We then used the Bayesian method of Arnold and Townend (2007) to infer the tectonic stress parameters for the earthquake swarm, incorporating an assumed error of $\pm 10^\circ$ in nodal-plane parameters. We separated moment-tensors into double couple and non-double couple to investigate whether there was any variation in stress parameters between the two types of earthquake. For the non-double couple moment tensors we

used the double couple component of the solution, as the stress inversion software does not allow for opening/closing modes.

We also investigate any possible ground deformation signals in the Taupō region using the GeoNet GNSS sensors. The GNSS data were analyzed using GAMIT/GLOBK version 10.71 (Herring et al., 2010), using over 100 global reference stations to evaluate daily site position in the IGB14 reference frame. We applied IGS14 absolute phase center models to all antennas and solved for site positions, satellite orbit, and Earth rotation parameters during the processing. We estimated the atmospheric zenith delay every two hours using the Vienna Mapping Function (VMF1) and corrected for higher order ionospheric refraction delay using IONosphere map EXchange formation (IONEX) files (Schaer, 1999). Ocean loading was removed using the Finite Element Solutions 2004 (FES2004) model (Lyard et al., 2006).

The GNSS time series spanning February 2012 to November 14 2016 were used to evaluate background deformation at each site (horizontal velocity, annual and semiannual variations for all [E, N, and U] components) which was then removed from the time series. In addition, we estimated and corrected for offsets due to antenna changes at sites TGHR, TGTK, and TGRA. Using six days before Swarm A (starting February 17, 2019) and six days after Swarm G (ending 07 September 2019) we then estimated the horizontal displacement at each site during Swarms A–G (Figure 10). We also estimated the displacement from October 2018 to the end of Swarm G, including the first 6 days of October. The vertical time series still showed significant annual variation after detrending. To remove any common mode non-volcanic signals we subtracted the TGHR vertical time series from all sites before evaluating the vertical displacement.

The GNSS data are then supplemented using the lake-leveling data from a platform at Horomatangi Reefs, which measures vertical uplift relative to a point outside the Taupō caldera and has estimated errors of 1.7–5.1 mm (Otway, 1986, 1987, 1989; Otway et al., 2002). These measurements were taken approximately every 3 months. We divided the geodetic data into two time periods; October 2018 through to the start of swarm A (February, 17 2019), and swarm A to the end of swarm G (September 8, 2019). After extracting the displacements spanning the two swarm periods, we estimate the location and volume change of a Mogi point source (Mogi, 1958) beneath the lake. Due to the limited number of observations and large uncertainties, rather than explicitly solve for a position and volume we generated a suite of forward models positioned at 1 km intervals covering the lake region at depths from 3 to 14 km (Figures S21 and S22). For each location, we solved for the volume change and assess the RMS misfit (Figures S21 and S22) allowing us to give an estimate of the best-fitting source region for the deformation.

4. Results

Earthquake activity at Taupō in 2019 predominantly occurred in seven distinct swarms (A–G), each with spatially distinct clusters and earthquake occurrence rates (Figure 3). Swarm A, which occurred between the February 17 and 21, featured five spatially discrete earthquake clusters, two clusters beneath the southern portion of the lake and three clusters to the south, northeast, and west of the Taupō caldera collapse structure (Figures 3 and S1). In total, swarm A featured 277 earthquakes ranging from M_L -0.4 to 2.5. It had absolute location errors of ± 1.55 km and ± 1.84 km for horizontal and vertical directions respectively, and relative errors of ± 0.59 km and ± 0.43 km for horizontal and vertical directions respectively. The southern clusters occurred between 3 and 9 km depth and were characterized by normal fault moment tensors, with rift-parallel strikes (NE-SW) that match the orientation of the clusters themselves (Figure S2). In contrast, the other three earthquake clusters occurred between 7 and 14 km depth and did not form linear structures. Moment tensors for these three clusters, though limited in number, suggested a non-double couple component (i.e., earthquake mechanisms differ from what is expected for slip on a fault-plane).

Swarm B (May 21) featured a single cluster of 501 earthquakes under the southern shore of the lake, with magnitudes ranging from M_L -0.7 to 2.8 (Figures 3 and S3). It had absolute location errors of ± 1.55 and ± 1.84 km for horizontal and vertical directions respectively, and relative errors of ± 0.71 and ± 0.46 km for horizontal and vertical directions respectively. The swarm predominantly occurred between 5.5 and 7.5 km depth on two ENE-WSW striking, structures. The earthquakes appeared to migrate ~ 1 km from the ENE to the WSW over a four-hour period and featured a mixture of double couple and non-double couple moment tensors (Figure S4). The first earthquake in the migratory sequence (2019p378968) had a

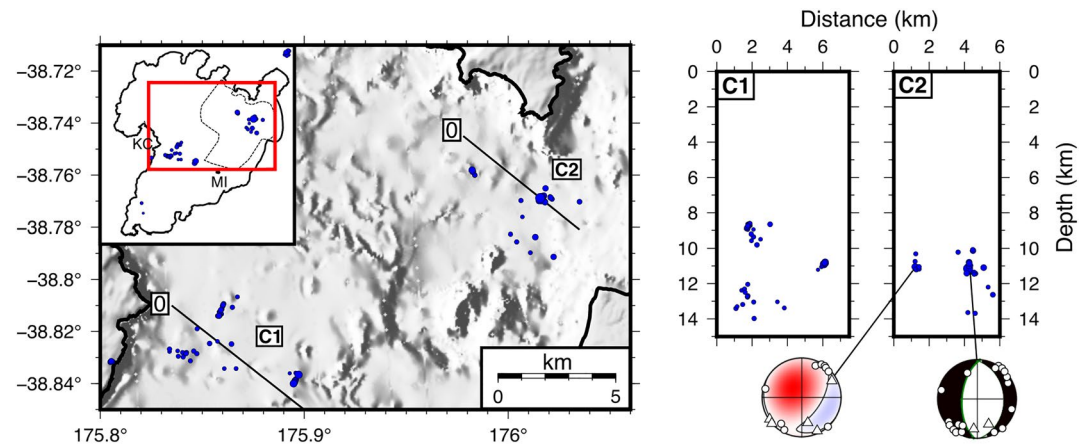


Figure 4. Map of the Lake Taupō area showing the locations of swarm C, which occurred between June 18 and 23. Red box in inset-map denotes location of main map panel. All cross-sections are plotted with a 1:1 scale. Selected moment-tensors are shown with a lower-hemisphere projection, individual polarity picks are represented by circles and triangles for compressional and dilatational phases respectively. Compressive and dilatational quadrants are black and white respectively for double-couple solutions, and red and blue respectively for non-double-couple solutions.

negative, horizontally aligned, tensile-crack moment tensor, while the following earthquakes were either; rift-aligned, normal-fault, double-couple events, or rift-aligned, sub-vertical, positive tensile-crack moment tensors (Figure S4).

Swarm C (June 18–23) featured 254 earthquakes with magnitudes ranging from M_L 0 to 3.2, the largest of which (2019p472013) caused widespread ground-shaking in Taupō town, coinciding with the rupture of a major sewer pipe on the waterfront in Taupō township (RNZ, 2019). It had absolute location errors of ± 1.39 km and ± 2.23 km for horizontal and vertical directions respectively, and relative errors of ± 0.52 km and ± 0.43 km for horizontal and vertical directions respectively. Swarm C consisted of two geographically distinct but temporally coincident clusters, one (Figure 4, C1) in the center of the lake between Motutai-ko Island and the Karangahape Cliffs, on the edge of the inferred Oruanui collapse collar boundary, and the other (Figure 4, C2) near the Taupō caldera collapse structure in the northeast of the lake. For both clusters the earthquakes were largely confined to depths of 8–14 km. Moment tensors showed that the southern cluster (C1) involved double couple earthquakes on rift-oriented fault planes. Conversely, the northeast cluster (C2) showed far more variation with the largest earthquake (2019p472013, M_L 3.17) presenting a double couple normal-fault moment tensor on a N-S oriented fault plane. There is, however, also evidence for non-double couple, positive tensile crack style earthquakes within this cluster (2019p469364, 2019p469374) (Figures 4 and S5).

Swarm D occurred between June 6 and July 7. This swarm featured 173 earthquakes ranging from M_L -0.7 to 3.2 and was almost entirely confined to offshore from the Karangahape Cliffs (Figure 5). It had absolute location errors of ± 1.15 km and ± 1.96 km for horizontal and vertical directions respectively, and relative errors of ± 0.46 km and ± 0.37 km for horizontal and vertical directions respectively. The earthquakes occurred over a range of depths from 3 to 14 km, but the majority of events occurred between 8 and 10 km depth. The calculated moment tensors displayed a mixture of double-couple and non-double-couple events. The double-couple earthquakes represented slip on either rift-aligned normal faults, NW-SE oriented vertical faults, or near-horizontal fault planes (Figure S6). The non-double-couple moment tensors all suggest deformation of sub-horizontal tensile cracks, with six out of seven calculated moment tensors representing a closing crack, mostly at depths of 8–10 km (Figures 5 and S6).

Swarm E immediately followed swarm D and continued through to July 13. It featured 328 earthquakes ranging from M_L -1.0 to 2.3 and was distributed in two clusters, one (E1) offshore from the Karangahape Cliffs in a similar location to swarm D, and the other (E2) below the northeast part of the lake (Figure 6). It had absolute location errors of ± 1.39 km and ± 2.06 km for horizontal and vertical directions respectively, and relative errors of ± 0.44 km and ± 0.39 km for horizontal and vertical directions respectively. Clusters

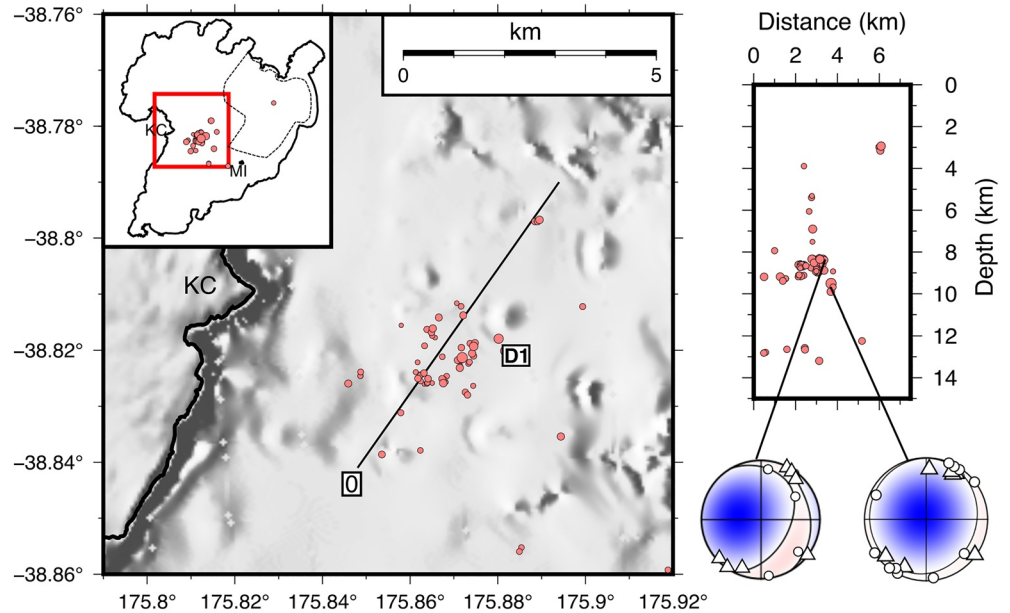


Figure 5. Map of the Lake Taupō area showing the locations of swarm D, which occurred between 06:00 on the June 6 and 15:00 on the June 7. Red box in inset-map denotes location of main map panel. All cross-sections are plotted with a 1:1 scale. Selected moment-tensors are shown with a lower-hemisphere projection, individual polarity picks are represented by circles and triangles for compressional and dilatational phases respectively. Compressive and dilatational quadrants are red and blue respectively for non-double-couple solutions.

E1 and E2 are largely distributed between 4 and 12 km depth, and the majority of calculated moment tensors are double-couple, but display a variety of fault-plane strikes and slip orientations (Figures 6 and S7). Cluster E1 consists of a horizontal plane of seismicity at ~11 km depth and an inclined plane between 8 and 11 km depth. Only one earthquake shows evidence for non-double-couple, positive tensile crack-style opening. In contrast, cluster E2 features discrete earthquakes with no clear structures discernible, with the earthquakes to the west clustering at 10–12 and 17 km depths and the earthquakes to the east occurring at 4–8 km depth.

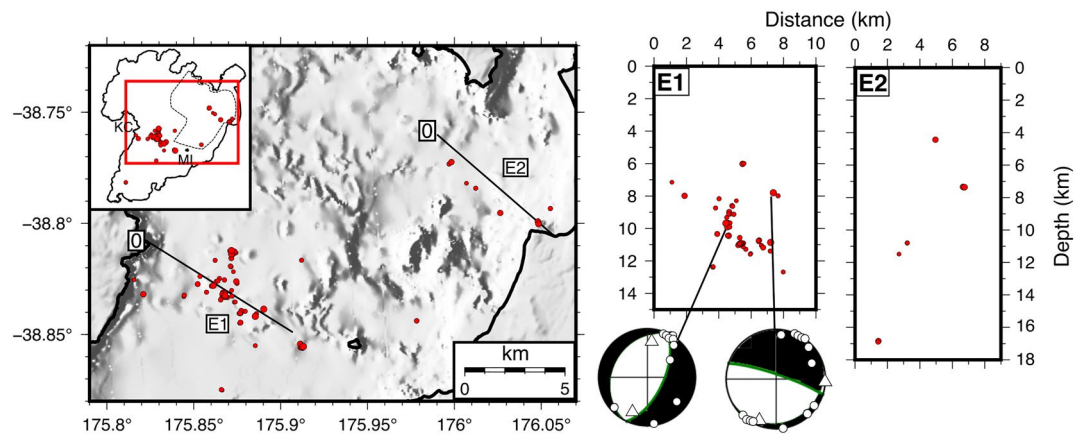


Figure 6. Map of the Lake Taupō area showing the locations of swarm E, which occurred between the July 7 and 13. Red box in inset-map denotes location of main map panel. All cross-sections are plotted with a 1:1 scale. Selected moment-tensors are shown with a lower-hemisphere projection, individual polarity picks are represented by circles and triangles for compressional and dilatational phases respectively. Compressive and dilatational quadrants are black and white respectively for double-couple solutions.

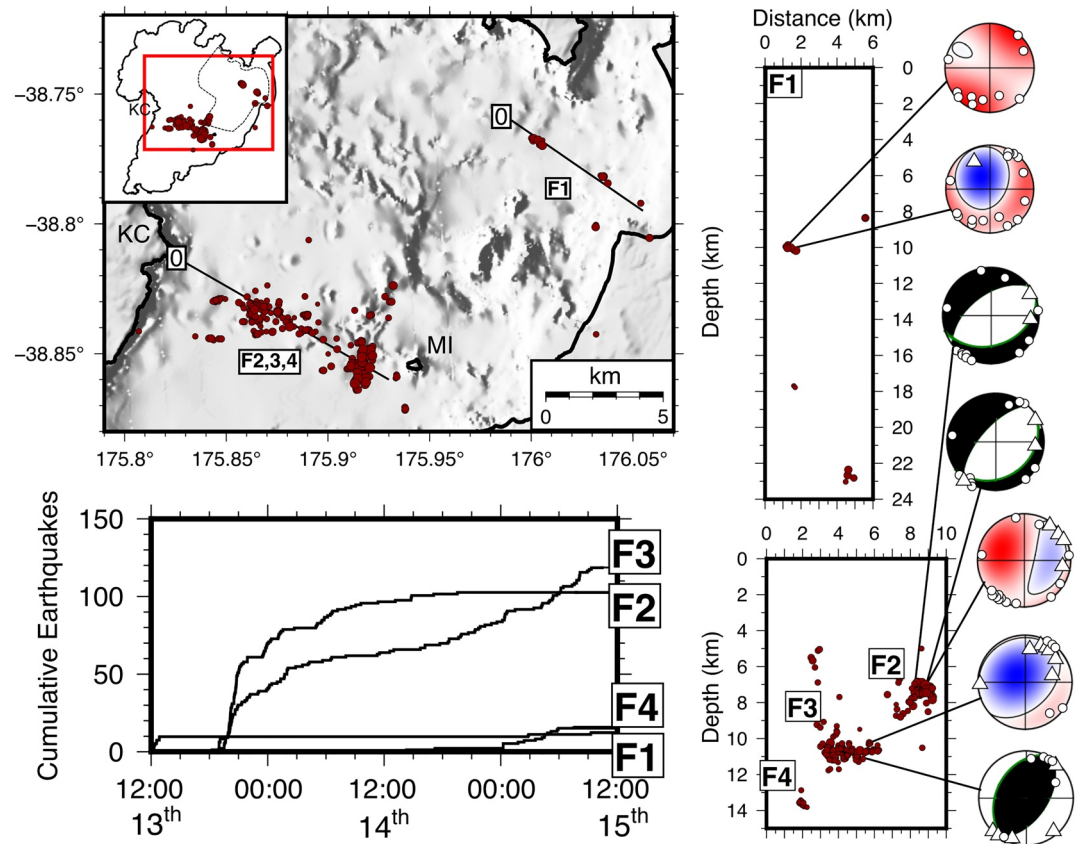


Figure 7. Map of the Lake Taupō area showing the locations of swarm F, which occurred between July 13 and 15. Red box in inset-map denotes location of main map panel. All cross-sections are plotted with a 1:1 scale. Selected moment-tensors are shown with a lower-hemisphere projection, individual polarity picks are represented by circles and triangles for compressional and dilatational phases respectively. Compressive and dilatational quadrants are black and white respectively for double-couple solutions, and red and blue respectively for non-double-couple solutions. Also shown is the cumulative number of earthquakes through time for each individual cluster, showing the progression of seismicity through time.

Swarm F then followed swarm E, lasted for ~ 48 h and featured 713 earthquakes ranging from M_L -0.1 to 3.1. It had absolute location errors of ± 1.49 km and ± 2.21 km for horizontal and vertical directions respectively, and relative errors of ± 0.52 km and ± 0.41 km for horizontal and vertical directions respectively. This swarm began with earthquake activity beneath the northeast part of the lake (cluster F1), which occurred over the space of ~ 1 h and featured earthquakes at 10 km depth and 22–23 km depth (Figure 7). Cluster F1 had three calculated moment-tensors, all from earthquakes at ~ 10 km depth, which were all non-double-couple and suggested volumetric expansion. Approximately 3 h later two spatially distinct clusters, F2 and F3, began. Cluster F2 occurred southwest of Motutaiko Island from 6 to 9 km depth and had no clear structure. Calculated moment-tensors show a combination of rift-aligned normal faults along with multiple non-double-couple moment tensors. Non-double-couple moment tensors all indicate volumetric expansion, apart from the last event that indicates closing (Figures 7 and S8). Cluster F2 lasted for ~ 18 h and ended around 12:00 on the July 14. Cluster F3 was in a similar location to cluster E1, toward the Karangahape Cliffs, but had rather different characteristics. This cluster can be subdivided into two separate structures. The first of these was active at the same time as cluster F2 and occurred along an inclined plane, ranging from 9 to 11.5 km depth, and was associated with a rift-aligned reverse fault moment-tensor (the only one of its kind in the 2019 activity; Figure 7). Earthquake activity in F3 showed a pattern of increasing depth and mirrored F2 by slowing in the activity toward 12:00 on July 14. There was then a resurgence in the activity in cluster F3, coincident with the halting of earthquakes in F2, but this activity was within a new, sub-horizontal structure at the base of the previously active inclined plane, at 10.5 km depth. The calculated

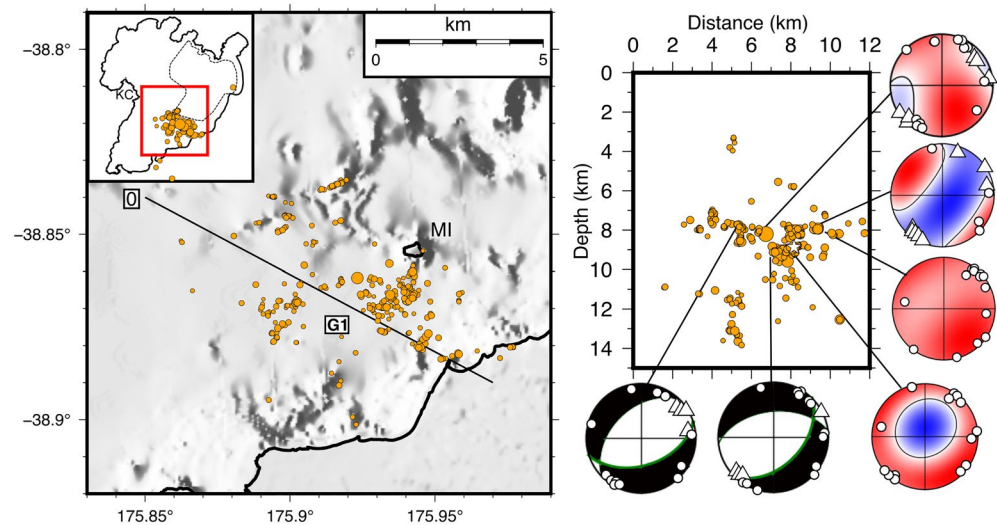


Figure 8. Map of the Lake Taupō area showing the locations of swarm G, which occurred between September 4 and 7. Red box in inset-map denotes location of main map panel. All cross-sections are plotted with a 1:1 scale. Selected moment-tensors are shown with a lower-hemisphere projection, individual polarity picks are represented by circles and triangles for compressional and dilatational phases respectively. Compressive and dilatational quadrants are black and white respectively for double-couple solutions, and red and blue respectively for non-double-couple solutions.

moment-tensors were all double-couple mechanisms except for the last two that indicated non-double-couple moment tensors suggesting negative volumetric changes (Figures 7 and S8). This resurgence in activity in cluster F3 also coincided with the emergence of cluster F4 at greater depths (13–14 km depth to the NW of F3, Figure 7).

Once swarm F had subsided there was essentially a hiatus in the seismic activity for the following 49 days prior to swarm G (Figure 3). Swarm G began on the evening of September 4 with a magnitude 5.3 earthquake (2019p665658) occurring ~1 km to the north of cluster F2 at ~8 km depth (Figure 8). This earthquake was widely felt throughout the North Island and caused a horizontal peak ground acceleration of 2.2% g (211 mm s^{-2}) in Turangi and minor damage (broken windows, fallen shelving) in villages near the Motuoapa peninsula and a landslide onto State Highway 1 near Hatepe, on the east of the lake (Bubs Smith, pers. comm.). This initial earthquake was then followed by 1171 earthquakes in the next 72 h, ranging from magnitudes M_L -0.1 to 3.7. It had absolute location errors of ± 1.21 km and ± 2.03 km for horizontal and vertical directions respectively, and relative errors of ± 0.6 km and ± 0.41 km for horizontal and vertical directions respectively. Earthquakes in swarm G occurred in multiple clusters across a depth range of 3–15 km, all of which initiated immediately after the M_L 5.3 earthquake. Swarm G had a combination of non-double-couple and double-couple moment tensors (Figure 8). The initial M_L 5.3 earthquake, along with other events in swarm G, was best constrained by the opening of a tensile crack. There were also multiple earthquakes, which had non-double-couple moment tensors suggesting explosive sources with no recorded dilatational phases (Figures 8 and S9). These were accompanied by many double-couple moment tensors, the majority of which were consistent with slip on rift-aligned normal faults (Figures 8 and S9). Unlike during swarms C, E, and F, there were only two coincident earthquakes beneath the northeast part of the lake during swarm G. Despite swarm G having a large (M_L 5.3) initial earthquake, the subsequent earthquake-rate did not follow the Omori-Utsu law typical for tectonic earthquakes and their aftershocks (Figure S10; Utsu et al., 1995).

The results of the stress inversion of calculated moment tensors showed a slight contrast between the stress field parameters for double-couple (74 events) and non-double-couple earthquakes (39 events) (Figure 9). The double-couple inversion returned stress parameters consistent with an extensional regime with a near-vertical S_{max} and SH_{max} oriented at 045° and a stress ratio (ν) of 0.7. In contrast the stress parameters returned from the non-double-couple inversion show a rotation of the stress field to a non-vertical S_{max} and non-horizontal S_{mid} , a rotation of SH_{max} to 033° and a stress ratio of 0.3.

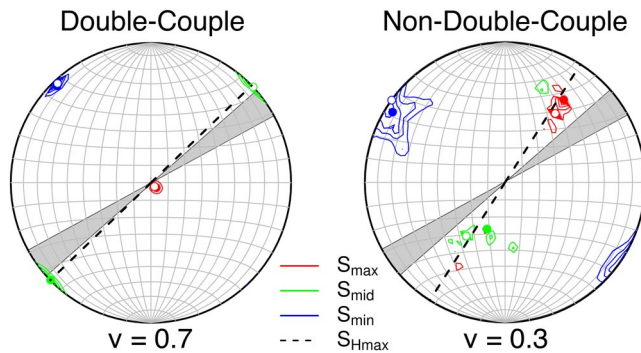


Figure 9. Stress inversion results from all 74 double-couple and 39 non-double-couple moment tensors, shown in lower-hemisphere projections. Colored contours represent the 90% confidence for the stress axes, ν denotes the stress-ratio. The shaded gray region shows the range of regional $S_{H_{max}}$ orientations (048° – 061°) from Townend et al. (2012) for comparison.

Our analysis of ground deformation observations shows that from October 2018 through to the beginning of swarm A appreciable horizontal deformation occurred at Horomatangi Reefs (TGHO) and Ouaha ridge (TGOH), with the two locations recording 6 and 4 mm of deformation respectively, both in a SE direction (Figures 10, S12 and S13). This was accompanied by small amounts of horizontal deformation at the other GNSS stations, which all radiate away from the center of Lake Taupō (Figure 10). During the time period of the earthquake swarms, we observed a continuation of the SE horizontal deformation at Horomatangi Reefs and Ouaha ridge (10 and 7 mm respectively), but this was also accompanied by 6 mm of vertical uplift at Horomatangi Reefs (Figures 10, S12 and S13). The inversion for a best-fit deformation source during the earthquake swarms suggests that an inflating body caused the observed deformation, ~ 1 km NW of Horomatangi Reefs (Figure 10). The best fit model is for an increase in volume of 3×10^{-3} km³ at 5 km depth with an R^2 value of 0.85, however a somewhat deeper source (5–8 km) is also permissible (Figure S22).

5. Discussion

The 2019 earthquakes and ground deformation represent the most significant period of activity to have occurred in the Taupō region for the past few decades, with >7000 earthquakes occurring, including a magnitude 5.3 earthquake being the largest event since 1952. Under the VUI system proposed by Potter, Scott, Jolly, Johnston, and Neall (2015) this activity at Taupō would be classified as “moderate unrest” with a classification score of 2.8, and thus the fifth unrest episode of this size recorded. In the following discussion we evaluate the nature of the 2019 unrest to better understand the driver(s) of seismicity and deformation, and discuss the implications for the modern magmatic system and ongoing monitoring of this active region.

5.1. Characteristics of the 2019 Unrest

The seven earthquake swarms (A–G) documented here show a wide range of characteristics that highlight the complexity of the 2019 unrest episode at Taupō volcano. Swarms A and B were distinct in their locations and earthquake characteristics from the swarms that followed. Swarm A was unique in that it featured four spatially distinct clusters (Figure S1). The cluster beneath the southern part of the lake (cluster A1), is inferred to be rift-related normal faults as it formed rift-aligned lineations and featured exclusively double-couple, rift-aligned normal faulting in the moment tensors (Figure S2). We therefore suggest that this southern cluster represents extensional faulting, typical of the TVZ (Rowland & Sibson, 2001; Villamor et al., 2017). We note, however, that seismicity extended to depths of ~ 8 – 9 km, which is near the base of the proposed seismogenic zone in the TVZ (Bryan et al., 1999), suggesting that the southern part of Lake Taupō has a relatively deep brittle-ductile transition (i.e., cooler crust). Swarm B featured earthquakes along a sub-vertical but diffuse plane which showed some evidence for lateral migration (Figure S3). The occurrence of non-double-couple earthquakes, alongside double-couple, suggests also the possible involvement of fluids with this swarm (Figure S4). The spatial distribution of earthquakes in swarm B was similar to those swarms observed elsewhere in the TVZ that have been ascribed to the ascent of magmatic/meteoric fluids along pre-existing structures (Bannister et al., 2016; Hayes et al., 2004; Reyners et al., 2007). Given that the south end of Lake Taupō hosts an active geothermal system (Tokaanu-Waihi; Figure 1; Bibby et al., 1995; Severne & Hochstein, 1994), we suggest that faulting accompanying the ascent of aqueous fluids is a likely explanation for swarm B.

Following swarms A and B, activity became focused beneath the center and northeastern part of Lake Taupō during swarms C–G. Swarms C–G shared many similar characteristics. They all had the majority of earthquakes occurring between Karangahape Cliffs and Motutaiko Island, while earthquakes often occurred contemporaneously in the NE of the caldera (Figures 4–8). When these swarms are taken together in map view, they form an approximate NW–SE trend between Karangahape Cliffs and Motutaiko Island, coincident with the inferred boundary of the Oruanui structural collapse caldera (Figure 1). The individual

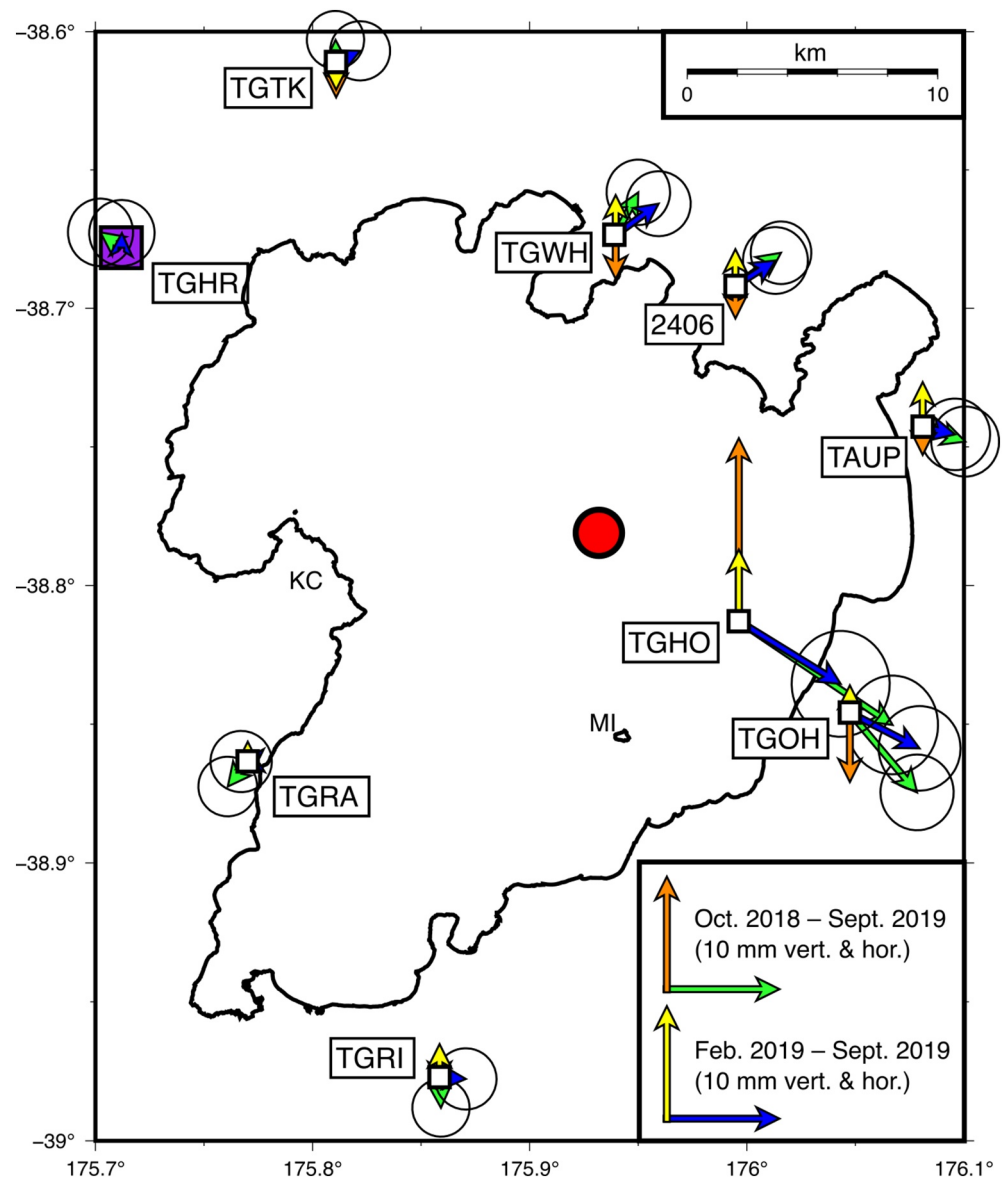


Figure 10. Map of the Lake Taupō area showing the locations of stations where the GNSS derived cumulative ground deformation was measured from October 2018 and during earthquake swarms A–G. Orange and green arrows show vertical and horizontal deformation vectors, respectively, for October 2018–September 2019. Yellow and blue arrows show vertical and horizontal deformation vectors, respectively, for February 2019–September 2019. Ellipses denote the error estimate. The purple square denotes GNSS station TGHR, which is used as a reference point. The red circle denotes the best-fit position of a model inflating deformation source. See Figures S13–S20 for the time-series data.

clusters within these swarms predominantly occurred at 7–9 km and ~11 km depths (Figure 11). These depths were also similar to those of earthquakes in the NE sector below the lake. However, earthquakes were not limited to these depths. For example, swarm F featured numerous earthquakes on a dipping plane between depths of 9–11 km and a small cluster at ~14 km depth while swarm G featured many earthquakes between 11 and 14 km depth (Figure 8).

Swarms C–G each featured a combination of double-couple and non-double-couple earthquakes. The majority of the non-double-couple earthquakes are best explained by opening tensile cracks, excluding swarm D and cluster F3 that are largely represented by closing tensile cracks. Swarms C–G show very little evidence for slip along fault-planes. The only evidence for this occurring was during the early stages of cluster F3 in swarm F (Figure 7), but the focal mechanism and spatial orientation of this stage of the cluster

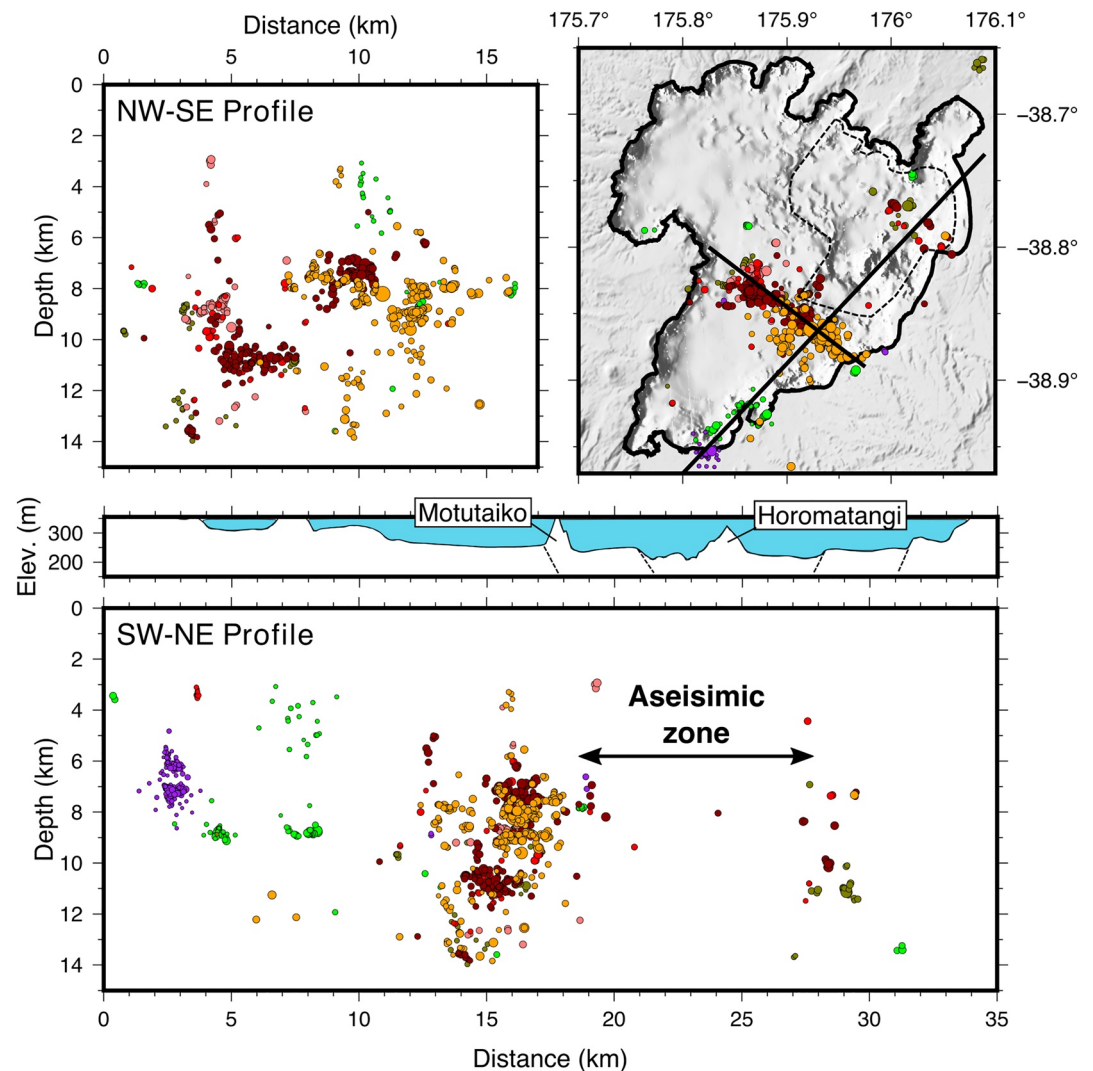


Figure 11. Map of and cross-sections through the 2019 Taupō seismicity, colored by individual swarm (Figure 3). Above the SW-NE profile is the bathymetry of the lake floor.

suggests that it was caused by reverse fault motion on a rift-oriented fault dipping at $\sim 70^\circ$. This unusual result is interpreted to reflect a reverse-reactivation of a rift-related normal fault. All other earthquake activity was characterized by sub-horizontal structures and non-double-couple moment tensors; hence the Swarms C–G in the 2019 earthquake activity cannot be explained by Taupō rift-related extensional faulting. In summary, the seismic activity at Taupō in 2019 showed a combination of rift-related normal faulting (sometimes fluid assisted) and repetitive clusters of earthquakes defining shallowly inclined features with non-double-couple moment tensors.

In addition to the elevated seismic activity, we find that there was significant ground deformation at Taupō which began in October 2018 and continued through to the end of swarm G. The deformation, which occurred during the earthquake activity is best explained by an inflating source at ~ 5 km depth (Figure 10). During swarms A–G, there is a distinct gap in seismic activity in the vicinity of the Horomatangi Reefs, and this aseismic zone corresponds to the location of the inferred inflating source.

5.2. Causes of the 2019 Unrest at Taupō

5.2.1. Rift Related Fault Slip?

The majority of earthquakes in the TVZ occur at depths of <6–8 km and this depth range is thought to approximate the brittle-ductile transition depth in this area of high heat flow (Bannister et al., 2016; Bryan et al., 1999). In comparison many of the 2019 Taupō earthquakes are deeper seated. While there are many double-couple earthquakes in the 2019 seismicity that are inferred to lie along rift-aligned normal faults, few of the earthquake clusters delineate inclined planes on rift-aligned lineations as one would expect for rift-related extensional faulting (e.g., Ebinger et al., 2019; Lavayssière, Drooff, et al., 2019; Lavayssière, Greenfield, et al., 2019; Muirhead et al., 2019). There are also multiple lines of evidence that suggest the 2019 earthquake swarms were associated with volumetric changes in the subsurface. First, swarms C–G all featured non-double-couple moment tensors, which suggest the closing (swarm D) or opening (swarms C, E–G) of tensile cracks. Such non-double-couple earthquakes have been shown experimentally to result from the involvement of aqueous fluids, and are inferred to arise from the movement of magma (Clarke et al., 2019). Second, swarm F featured cluster F3, which is interpreted to reflect the reactivation of a normal fault plane in a reverse sense. This is evidenced by the reverse fault moment tensor within a plane of seismicity dipping at $\sim 70^\circ$, which was then followed by a sub-horizontal swarm of earthquakes at the base of the fault plane (Figure 7). We suggest that cluster F3 was caused by the inflation of a sub-horizontal body within the hanging-wall of a rift-related normal fault, which then reactivated the fault in a reverse sense. Third, by using moment tensors to invert for stress field parameters, we found that the non-double-couple earthquakes are associated with a rotated and non-Andersonian stress field, when compared with the double-couple earthquakes (Figure 9). While the stress field driving the double-couple earthquakes is consistent with the extensional environment, and previous studies from the TVZ (Townend et al., 2012), the non-double-couple earthquakes appear to be arising from a locally rotated stress field. Fourth, we find that the earthquake-rate-decay following the magnitude 5.3 earthquake in swarm G does not follow the Omori-Utsu law (Figure S10; Utsu et al., 1995), suggesting that this large earthquake was not tectonic in origin. Fifth, vertical GNSS measurements and the lake-leveling data at Horomatangi Reefs, the only geodetic measurements within the caldera, show that uplift occurred during the earthquake swarms (Figures 10 and S12). These observations combine to suggest that the majority of the earthquake activity in 2019 was not primarily caused by rift-related faulting, but rather was controlled by the movement of fluids (water and/or magma).

5.2.2. Migration of Magma or Aqueous Fluids?

As previously discussed, seismic swarms in volcanic areas worldwide have been attributed to the migration of magma or aqueous fluids along structural features (e.g., faults) acting as a permeable pathway (Bannister et al., 2016; Greenfield et al., 2019; Hotovec-Ellis et al., 2018; Reyners et al., 2007; Shelly et al., 2015). This behavior causes earthquake clusters that clearly delineate the fault structure, and tend to migrate vertically upwards. We suggest that aqueous fluid movement may have controlled swarm B, as this delineated an approximately SW-NE trending fault and there was a migration of earthquakes (Figures S3 and S4). However, as previously mentioned, there was very little evidence in swarms C–G for fault-like structures, and the one cluster that did show such evidence (swarm F/cluster F3) had earthquakes that deepened along the fault structure through time (Figure 7). Therefore, we do not see evidence that the earthquakes in swarms C–G were primarily caused by the response of regional tectonic faults to the migration of aqueous fluids.

5.2.3. Magma Intrusion Events?

Repeated, stalled intrusions are inferred to commonly occur at silicic caldera volcanoes and can generate a wide range of unrest signals (Acocella et al., 2015). For the reasons discussed below, we infer that magmatic intrusions were an integral part of the 2019 events at Taupō. For swarms C, E, and F, one of the most outstanding features was the contemporaneous seismicity in the NE and SE margins of the caldera, occurring over similar depth ranges (Figures 4, 6, and 7). The contemporaneous nature of the seismicity suggested that there was some physical or indirect connection between the two regions, despite the ~ 10 km gap between them in which area there was very little seismicity throughout the entire unrest period (Figures 11 and 13). Interestingly, the surface projection of this aseismic region coincides with the vent locations for recent (<2.2 ka) eruptions from Taupō (Figure 1; Barker et al., 2016; Wilson, 1993), a large negative gravity anomaly

interpreted to arise from caldera collapse following these previous eruptions (Davy & Caldwell, 1998), elevated heat flow (Whiteford, 1996), and active hydrothermal venting (de Ronde et al., 2002). This region is therefore considered to be the most likely location for the modern day focus of magmatism (Barker et al., 2019, 2021). It is possible that magmatic intrusion and/or deformation was occurring in this region, but in an aseismic fashion due to high crustal temperatures, as has been observed in Hawaii and Japan (Janiszewski et al., 2020; Uchide et al., 2016; Wright & Klein, 2006). This is supported by ground deformation that occurred at the GNSS sensors and lake-leveling station in 2019 (Figures 10 and S12–S19). This deformation started a few months prior to the seismic activity but ceased around the same time.

Our forward models show that the observed pattern of vertical and horizontal deformation can be explained by an inflating body, ~1 km NW of Horomatangi Reefs, at 5 km depth (Figure 10). We therefore suggest a model in which the deformation at Taupō was caused by the inflation of a magma body to the NW of Horomatangi Reefs, starting October 2018–September 2019. This inflation was contemporaneous with the earthquake activity that was occurring at both the NE and SW edges of the broader magma reservoir (Figure 13). We suggest that the reason for this seismicity distribution is that in the aseismic region below the Horomatangi Reefs the brittle-ductile transition is very shallow due to the presence of a large magma reservoir, as further discussed as given below:

5.3. Implications for the State of the Modern Magma Reservoir

With the presence of Lake Taupō inhibiting detailed geophysical surveys, most of the insights into the Taupō's magmatic system have been provided by petrological studies of past eruptive products (Allan et al., 2017; Barker et al., 2014; 2015; 2016; Sutton et al., 2000). Taupō has been highly active since 12 ka, with at least 25 eruptions, mostly vented along the eastern side of the lake (Barker et al., 2019; Wilson, 1993). Petrological studies of the magmas erupted during this period provide insights into several key features of the Taupō's magmatic system.

1. *Repeated extraction of crystal-poor rhyolites.* The young eruption products from Taupō during the Holocene are overwhelmingly crystal poor (<5–7 wt. %) rhyolites that show very little intra- or inter-eruptive compositional variations despite a wide distribution of vent sites and magma volumes spanning <0.01–35 km³ (Barker et al., 2015). These crystal poor rhyolites were extracted from a long-lived crystal rich mush reservoir and assembled as a melt-dominant body only shortly prior to eruption. For example, diffusion timescales preserved in orthopyroxene crystals from the 1.8 ka Taupō eruption indicate that melt accumulation occurred in only years to decades prior to eruption, following heating of the crystal mush in the preceding decades to centuries before the eruption (Barker et al., 2016). The primary mechanisms driving melt extraction from the mush are still uncertain as the majority of other Holocene eruptions show no evidence for mafic magma triggering, but tectonic processes likely are a critical control on the production and eruption of melt bodies of varying size (Barker et al., 2021; Rowland et al., 2010). The high geothermal heat flux at Taupō suggests that the melt-dominant bodies have a short lifespan for eruption before they cool and crystallize back to melt-poor mush, and it seems inevitable that many more transient, unerupted bodies have been created during the last 12 kyr.
2. *Conditions of magma storage.* Taupō's magmas show step-wise changes in chemical composition through time, reflecting changing mineral stability due to minor changes in storage conditions (e.g., temperature, H₂O content, and oxygen fugacity or pressure: Barker et al., 2014, 2015). Inheritance of crystals (zircons; plagioclase and orthopyroxene cores) between eruptions indicates that these magmas were sourced from an evolving mush that in its youngest history likely resides at temperatures of >750°C between eruptive periods (Barker et al., 2014). Storage pressures from melt inclusion H₂O/CO₂ contents (e.g., Dunbar et al., 1989; Myers et al., 2018, 2019) and/or mineral barometry from young eruptives indicate that the crystal-poor magmas that erupted were assembled at depths of 5–8 km (Barker et al., 2015). Deeper magmas are likely to be dacitic or intermediate in composition, which are in turn fed by mafic magmas intruding into the ~15 km-thick quartzofeldspathic crust in this region of the TVZ (Stern & Benson, 2011).
3. *The extent of the modern magmatic system.* Using the vent spacing and inferred crystallization depths, Barker et al. (2015) estimated the volume of the modern silicic magmatic system to be between 250 and 1000 km³. However, this estimate is only a first-order calculation and does not take into account the lateral movement of magmas, which is thought to be potentially important in this rifted setting (Allan

et al., 2012; Benson et al., 2021; Wilson et al., 2009). The minimum geographic areas of the magmatic system is determined by the collapse structure that formed during the 232 CE Taupō eruption, which is also the area of most intense modern heat flow on the lake floor (Davy & Caldwell, 1998; de Ronde et al., 2002; Whiteford, 1996).

When these features are taken into consideration, the presence and locations of the 2019 earthquake swarms provide new additional insights into the state of the modern magmatic system at Taupō, as further outlined below.

5.3.1. Conditions in the Reservoir

The 2019 earthquake swarms predominantly occurred along the southern margin of the Oruanui structural caldera, with a relatively smaller number of events occurring at the same time beneath the northeastern corner of the lake in a region that also coincides with a steeper gradient in the gravity anomalies (Davy & Caldwell, 1998; Wilson, 2001). The spatial locations and depths of the swarms in the mid crust (>5 km) outline and surround the inferred margins of the modern magmatic system (Barker et al., 2015, 2021). In contrast, little seismic activity occurred in the region where the modern magma system is inferred to lie. Seismic gaps or “shadow zones” are commonly observed beneath volcanoes in regions where significant amounts of partial melt are thought to occur (Janiszewski et al., 2020; Uchide et al., 2016; Wright & Klein, 2006), reflecting an altered rock deformation behavior from brittle to ductile as a function of temperature (Ebinger et al., 2008; Magee et al., 2018). To investigate the relationships between the lack of seismicity in the middle of Lake Taupō and possible magma reservoir conditions, we considered the brittle to ductile transition in rhyolite magmas as observed in experimental studies (Supporting File 1; Wadsworth et al., 2018). Such experimental studies have shown that in viscous, crystal bearing magmas, wholesale fracturing can occur under certain conditions (Dingwell, 1996; Cordonnier et al., 2012). Elastic shear stresses are stored or relaxed in fluids whereby relaxation occurs over a characteristic relaxation time:

$$\lambda_r = \frac{\mu}{G_\infty}, \quad (3)$$

where μ is the suspension viscosity and G_∞ is the elastic shear modulus. This relaxation time can be compared with the timescale of deformation λ , which can be taken to be the inverse of the strain rate $\dot{\lambda} = \dot{\gamma}^{-1}$. This comparison yields a dimensionless strain rate, or a scale independent Weissenberg number:

$$Wi = \lambda_r \dot{\gamma} = \frac{\mu}{G_\infty} \dot{\gamma}, \quad (4)$$

Wadsworth et al. (2018) adapted Eq. 4 for the additional effect of crystals, and found that, in general, $0.01 < Wi < 0.04$ represents a transitional window from viscous to brittle behaviour in crystal-bearing silicic magmas. Viscosity is strongly dependent on temperature (T) and can be predicted using empirical models that account for liquid composition and dissolved volatile concentration (C_{H_2O} ; Hess & Dingwell, 1996). We use composition of Taupō magmas from previous eruptions (Barker et al., 2015) across a range of temperatures and crystallinities (constrained by rhyolite-MELTS thermodynamic models: Gualda et al., 2012) to calculate suspension viscosity (Table S1; Hess & Dingwell, 1996; Maron & Pierce, 1956). Using rheological constraints from experimental studies of silicic magmas (e.g., Caricchi et al., 2007; Cordonnier et al., 2012; Mueller et al., 2010; Wadsworth et al., 2018) we then calculate the mode of deformation across a range of strain rates (Figure 12), where $0.01 < Wi < 0.04$ represents the transition from viscous to brittle behavior. The mode of deformation of crystal-rich magmas is largely dependent on the maximum crystal content at rheological locking (Mueller et al., 2010) and here, we use a conservative maximum crystal content of 80% (Caricchi et al., 2007). Figure 12 highlights that Taupō silicic magmas containing >20%–30% melt will only experience brittle failure at very high strain rates (e.g., $>10^{-1} \text{ s}^{-1}$) that would only be associated with fault rupture directly propagating into the magma reservoir (Rowe et al., 2011). Lower strain rates associated with tectonic loading (e.g., $<10^{-3} \text{ s}^{-1}$) or intrusion (e.g., $<10^{-6} \text{ s}^{-1}$) (Petford & Koenders, 2003) are not sufficient to cause brittle deformation at melt volumes exceeding 20%–30%. We therefore suggest that the seismic gap observed at Taupo represents a region of the magmatic system that contains a minimum of 20%–30% melt.

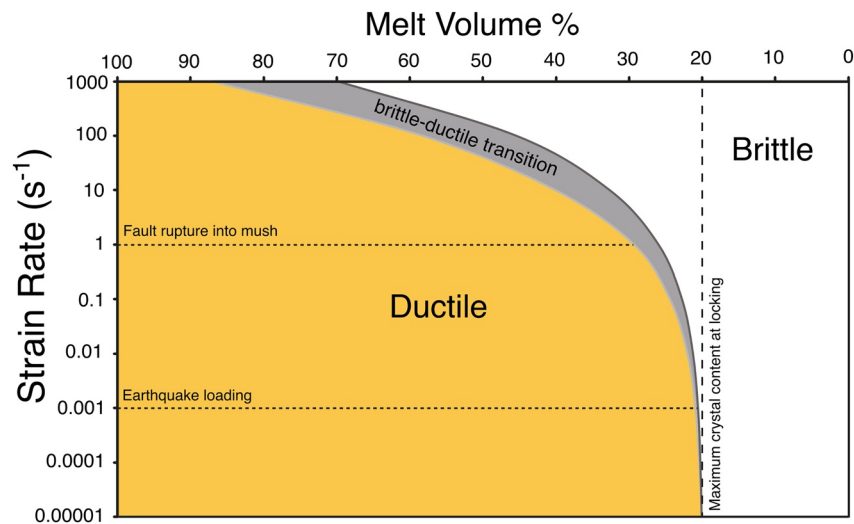


Figure 12. Diagram showing the range of strain rates over which rhyolite magma from Taupō is expected to show either brittle or ductile modes of deformation across a range of melt contents. The area highlighted in gray represents the region where $0.01 < Wi < 0.04$ and denotes the transitional window from viscous to brittle behavior (Wadsworth et al., 2018). Calculations assume a maximum packing of 80% crystals (Caricchi et al., 2007). Crystal contents and temperatures are calculated from Rhyolite-MELTS (Gualda et al., 2012) for magma compositions from the 1.8 ka Taupō eruption at 4.5 wt. % H_2O (Barker et al., 2015). Dotted horizontal lines highlight the range of strain rates that would be expected from different mechanisms. Earthquake loading strain rates are from Petford & Koenders (2003) and fault rupture strain rates are considered to be a maximum for the fault slip of 1 m/s for a fault plane of >30 cm thickness (Rowe et al., 2011). See Supporting File 1 for further details.

5.3.2. Nature and Extent of the Modern Magmatic Reservoir

The patterns of seismicity at Taupō during 2019 highlights three important aspects around the conditions of the mush reservoir. First, the main magmatic system where the seismic gap occurs is inferred to incorporate at least 20%–30% (or more) of melt, such that strain associated with intrusion can effectively be accommodated by ductile deformation. Second, the clustering of earthquakes to the SW and NE likely define the edge of the magmatic system and the ductile to brittle transition, where any magma has $<20\%$ –30% melt associated with lower temperatures across the interface between the magmatic system and host country rocks (e.g., Barker et al., 2014; Charlier et al., 2010). Third, with increasing distance away from the reservoir, this brittle-ductile transition appears to continue to greater depths such that there is a near-vertical rheological boundary at the SW and NE edges of the reservoir (Figure 13). Therefore, while intrusion(s) may occur aseismically beneath Horomatangi Reefs, once the associated strain reaches this boundary the crust is cool enough to facilitate brittle fracturing and earthquakes (e.g., Schofield et al., 2012). This may also explain why we see ground deformation beginning prior to the onset of seismicity. We can see this transition in a three-dimensional sense by examining the distribution of earthquakes in both a NE-SW and SW-NE orientation (Figure 11). In an along-rift SW-NE projection, the earthquake distribution suggests that between 5 and 8 km depth the vertical brittle-ductile/compositional transition occurs beneath Motutaiko Island (17–19 km distance on Profile 2; Figure 11), but at depths of 8–12 km, the transition occurs further SW with very little seismicity beneath Motutaiko Island. In contrast, to the NE the vertical brittle-ductile/compositional transition occurs at a consistent 28–30 km distance on Profile 2 on Figure 11. It is possible there is a similar brittle-ductile/compositional boundary at 8–12 km depth to the NW of Motutaiko Island (10–12 km distance on Profile 1; Figure 11). These observations suggest that there is a rift-aligned region which is able to sustain aseismic deformation between 8 and 12 km depth, which extends from the NE of the caldera (28–30 km distance on the SW-NE projection; Figures 11 and 13) to (at the farthest) the region that sustains brittle faulting in swarm A (10 km distance on SW-NE projection; Figure 11). This region is interpreted to be a locus of lower-crustal intrusions.

If the 2019 seismicity is considered to be outlining the outer edges of the mushy magma reservoir, a first-order estimate can be placed on its volume. The aseismic area is relatively well defined in a NE-SW direction

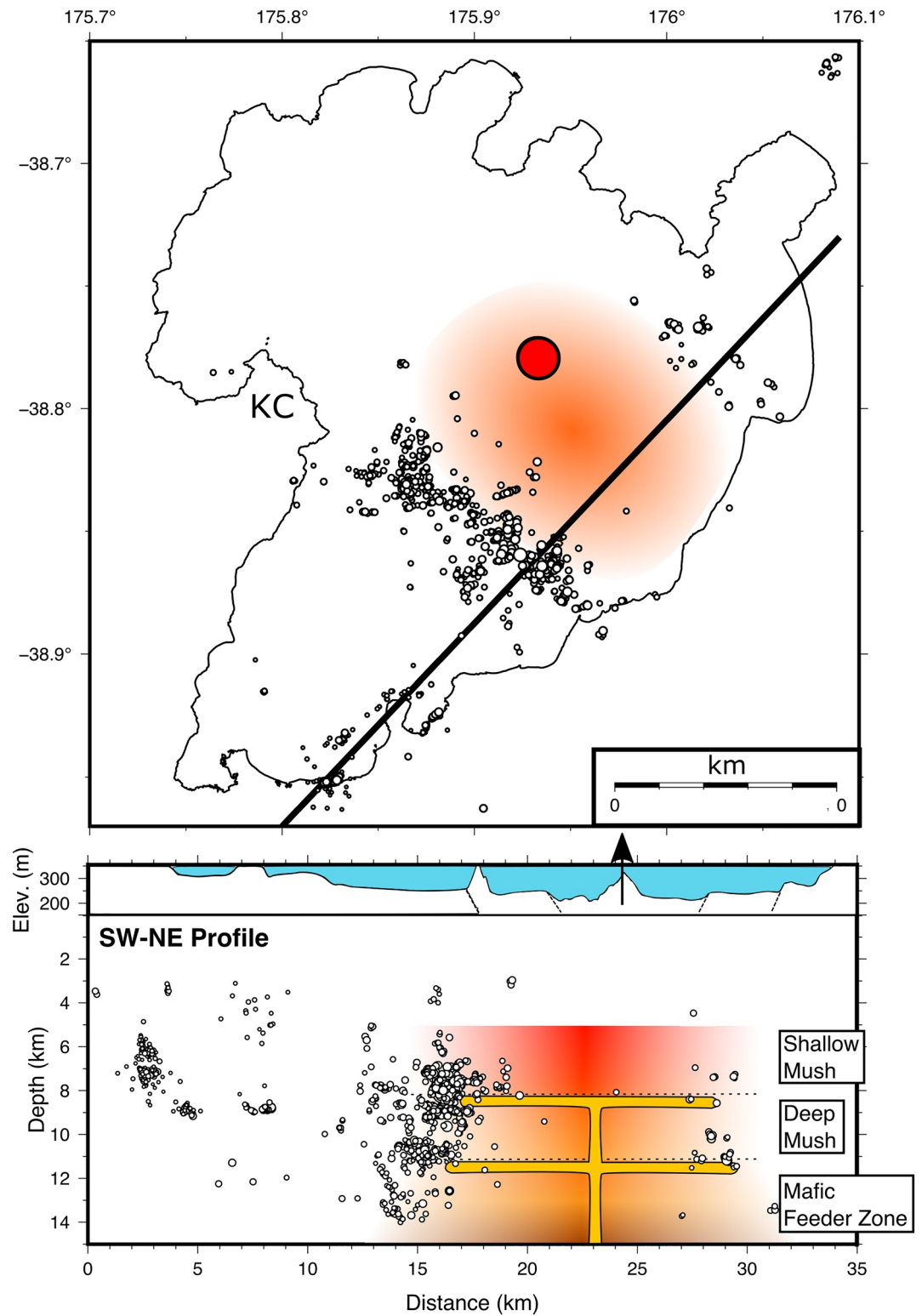


Figure 13. Map of Lake Taupō, showing the inferred location of the volcano’s magma reservoir which is estimated to have >20%–30% partial melt, see text for discussion. The red circle in map view denotes the best-fit location of the inflating source responsible for the observed ground deformation (Figure 10). Cross section shows all earthquakes considered here from the 2019 activity, projected on to a rift-parallel line along with a schematic representation of the mush zone. See text for explanations of the layers within the mush zone.

~5 km either side of Horomatangi Reefs. However, to the NW and SE the scarcity of earthquakes mean that these boundaries are less well defined (Figures 11 and 13). Two Holocene vents near Ouaha Ridge on the eastern side of Lake Taupō likely define the outer edge of the reservoir in this direction (Barker et al., 2015). No 2019 uplift was observed beneath the GNSS station on Ouaha Ridge but a small number of earthquakes occurred beneath this region in 2019. To the NW of Horomatangi Reefs no deep seismicity was observed in all of 2019 and therefore the western extent of the reservoir is undefined. We therefore suggest that a minimum area for the modern magmatic reservoir is ~80 km², with a maximum area possibly exceeding 250 km² suggested by the lack of seismicity to the west. Further studies of deep earthquake locations or geophysical imaging of the crust will be needed to confirm this western boundary (Illsley-Kemp et al., 2020).

A notable feature of the 2019 earthquake swarms is that they collectively defined domains of more intense seismicity at particular depths in the crust spanning the mid to lower crust from >5 to 15 km depth (Figure 11). We suggest that these domains could potentially reflect compositional boundaries within the magmatic system. The earthquakes defining these domains occur at two rather distinct depths, 7–8 and 11 km, there were then two more diffuse regions of seismicity from 5–8 and 11–15 km depth (Figure 11). If the earthquake swarms were occurring at the edges of sills, this suggests that there could have been ponding of magma at 7–9 and 11 km depth. Ponding of magma can be caused by density contrasts between the injected melt and the host magmatic system as commonly inferred from field examples of plutonic rocks (e.g., Bain et al., 2013) and numerical modeling (Carrara et al., 2020). Notably, these depths overlapped, within error, with the inferred depths of the shallow silicic mush (5–8 km) and deeper mush as inferred from compositional characteristics of erupted magmas at Taupō (Barker et al., 2015, 2021). The depth range of the earthquakes allows some further constraints to be placed on the volume of the magma reservoir using the extent of the aseismic region. Assuming that the shallow rhyolitic system spans a depth range of 5–8 km (Barker et al., 2015), a minimum volume of crystal mush of ~250 km³ is calculated, which in-turn is fueled by an even larger, less evolved mush at greater depths. Assuming a minimum of 20%–30% melt from this aseismic region (Figure 12), up to ~60 km³ of rhyolite melt could be present. However, with the unknown extent of the magmatic system to the west, we highlight that the volumes of interstitial melt calculated are minima (Figure 13).

5.4. Nature of the Unrest at Taupō and Implications for Monitoring

The nature of what constitutes “volcanic unrest” and how it might be responded to at a volcano like Taupō collectively pose several challenges. The very definition of volcanic unrest requires it to be a direct result of disturbances in the magmatic system, yet the setting of Taupō in a rift system, widening at 8–10 mm/yr in this area (Wallace et al., 2004; Villamor et al., 2017) makes delineating tectonic versus magmatic causes for enhanced seismicity and deformation difficult. Concealment of the young vent areas beneath Lake Taupō precludes the utility of conventional monitoring techniques such as fluid discharge volumes and chemistries and limits intra-caldera surface deformation measurements to the single site at Horomatangi Reefs. Prior episodes of an unusual seismic activity and/or deformation at Taupō, although treated individually and collectively as volcanic unrest (Potter, Scott, Jolly, Johnston, & Neall, 2015; Potter, Scott, Jolly, Neall, & Johnston, 2015) could not be uniquely fingerprinted as reflecting disturbances of the magmatic system. We have demonstrated that the 2019 events involved processes of disturbance to the Taupō magmatic system and as such represented true volcanic unrest.

The magmatic system below Taupō (see previous section) is, like many other rhyolitic systems worldwide, inferred to spend most of its history as a relatively immobile crystal-rich mush (e.g., Bachmann & Huber, 2016). Magma that has been erupted at Taupō is generally crystal-poor, and so prior to each eruption there is implied to be a period of segregation of melt (plus some crystals) into a holding body, which would inherently constitute volcanic unrest. However, it is likely that the processes leading to segregation of melt-dominant magma occur much more frequently than do eruptions, with the segregated magma rapidly cooling back to mush. At one extreme, in the case of the giant magma body that fed the ~530 km³ 25.5 ka Oruanui eruption, the crystal-poor magma body grew over a period of only ~600 years, and yet was cooling by several tens of degrees centigrade during that time (Allan et al., 2017). The viable lifetime of smaller bodies can be inferred to be proportionately shorter (Barker et al., 2016), such that an additional factor is inferred (principally tectonics: Rowland et al., 2010) to be involved that causes these bodies to be erupted

on an average recurrence interval of ~900 years, but varying greatly from ~10 to 20 years to ~5,000 years (Wilson, 1993). Thus any unrest event that can be demonstrated to involve magma movement and segregation, as with the 2019 unrest, can be inferred to represent a potential eruption. While it is far more likely that unrest events will not lead to an eruption, identifying the tipping-points and associated signals, which may indicate an impending eruption is a vital research area for Taupō and caldera volcanoes worldwide.

The 2019 events at Taupō thus raise several issues around monitoring of the volcano and assessing its state in terms of the alert level system used by GeoNet in its monitoring program (Potter et al., 2014). Placed in the context of previous events at Taupō, the 2019 event would rate as 2.8 on the VUI (Potter, Scott, Jolly, Johnston, & Neall, 2015; Potter, Scott, Jolly, Neall, & Johnston, 2015). However, there are several issues in use with the VUI with the allocation of unrest phenomena. For example, earthquake swarms or hydrothermal eruptions at the nearby Wairakei-Tauhara geothermal field may be attributed to Taupō volcano despite involving wholly separate phenomena. In New Zealand, volcanic alert levels, defined by GNS Science (Potter et al., 2014), range from 0 to 5 with 0 representing “no volcanic unrest” 1 and 2 representing “minor” and “moderate to heightened” volcanic unrest respectively, and levels 3–5 representing eruptions of increasing size. An expert panel using the latest data from the GeoNet monitoring network decides upon the alert level of any given volcano. The 2019 activity did not result in the volcano alert level for Taupō being raised from its (up until now) unchanging value of 0. In July and September 2019, after swarms F and G respectively, GeoNet released public statements stating that there were no indications that the earthquake activity was related to unrest in Taupō’s magmatic system. It can be posited that if the finding from our analysis had been available in near real-time then the alert level could/should have been raised to alert level 1 (i.e., minor volcanic unrest), particularly during swarm G. However, given the duration of the overall unrest episode and the non-volcanic signals at its onset, coupled with perceptions about the nature of the volcano and its eruptive potential, the timing and handling of any raising and lowering of the alert level would have been challenging. Future public engagement and education initiatives can play a key role in demystifying unrest at this inherently restless volcano.

In addition, although this study utilized the publicly available data from GeoNet, the time required for analysis and interpretation of these records at present makes rapid responses to the monitoring the data difficult. Further considerations on better tracking any unrest associated with magmatic processes at Taupō are hampered by the presence of the lake. This restricts measurements of intra-caldera surface deformation to the single point at Horomatangi Reefs, limits assessment of any changes in the chemistry of discharged fluids from the active hydrothermal system (de Ronde et al., 2002) and precludes seismic and geodetic monitoring directly above the inferred earthquake sources. We suggest that consideration be given to how this and other caldera volcanoes where large areas are concealed beneath lakes might be more efficiently monitored, and in particular how seismic and geodetic events might be accurately located and characterized in order to be able to provide realistic responses to future unrest events of this type.

6. Conclusions

Through detailed analysis of seismic activity and ground deformation, we have shown that from March to September 2019 Taupō volcano underwent a period of volcanic unrest, most likely associated with the intrusion of magma into the long-lived silicic magma mush reservoir. Ground deformation shows that this intrusion may have begun in October 2018. The seismicity associated with this volcanic unrest serves to delineate the boundaries of the silicic mush and we estimate that there is at least 250 km³ of mush with a minimum of 20%–30% melt fraction between 5 and 8 km depth beneath the present day Horomatangi Reefs. The 2019 volcanic unrest at Taupō showed that this is an active volcano and that even non-eruptive unrest can pose hazards to local communities. Future improvements to the monitoring network, particularly within the lake, could greatly advance our understanding and capability to rapidly respond to future unrest episodes.

Data Availability Statement

The authors also acknowledge GeoNet (geonet.org.nz), who provided all of the seismic and GNSS data used in this study through their public website, and are funded by the Earthquake Commission and GNS Science. All the seismic and geodetic data used in this study are freely available from GeoNet and the associated datasets can be found at <https://doi.org/10.5281/zenodo.4595831>.

Acknowledgments

F. Illsley-Kemp, S. J. Barker, C. J. N. Wilson, S. Ellis, I. J. Hamling, E. R. H. Mestel, and M. K. Savage are supported by the ECLIPSE program, which is funded by the New Zealand Ministry of Business, Innovation and Employment (MBIE). F. Illsley-Kemp and C. J. Chamberlain are supported by the New Zealand Earthquake Commission Programme in Earthquake Seismology and Tectonic Geodesy at Victoria University of Wellington. S. J. Barker is supported by the Marsden Fund of the Royal Society of New Zealand (grant VUW1627). This project utilized the following open-source software, for which we thank the authors: Obspy (Beyreuther et al., 2010), PyRocko (Heimann et al., 2017), EQcorrscan (Chamberlain et al., 2018), Matplotlib (Hunter, 2007), GMT (Wessel et al., 2019) and the Scientific Color Maps (Crameri, 2021). All digital elevation models use data from the Shuttle Radar Topography Mission (SRTM). The authors also wish to acknowledge the use of New Zealand eScience Infrastructure (NeSI) high performance computing facilities for this research. New Zealand's national facilities are provided by NeSI and funded jointly by NeSI's collaborator institutions and through the MBIE Research Infrastructure program. The authors thank Graham Leonard and Peter Otway for useful discussions. We are also grateful for two constructive and detailed reviews from Luca De Siena and Sarah-Jaye Oliva, which helped to improve the manuscript.

References

Acocella, V., Di Lorenzo, R., Newhall, C., & Scandone, R. (2015). An overview of recent (1988 to 2014) caldera unrest: Knowledge and perspectives. *Reviews of Geophysics*, 53(3), 896–955. <https://doi.org/10.1002/2015RG000492>

Allan, A. S. R., Barker, S. J., Millet, M.-A., Morgan, D. J., Rooyakkers, S. M., Schipper, C. I., & Wilson, C. J. N. (2017). A cascade of magmatic events during the assembly and eruption of a super-sized magma body. *Contributions to Mineralogy and Petrology*, 172(7), 49. <https://doi.org/10.1007/s00410-017-1367-8>

Allan, A. S. R., Wilson, C. J. N., Millet, M.-A., & Wysoczanski, R. J. (2012). The invisible hand: Tectonic triggering and modulation of a rhyolitic supereruption. *Geology*, 40(6), 563–566. <https://doi.org/10.1130/G32969.1>

Anderson, J., & Wood, H. O. (1925). Description and theory of the torsion seismometer. *Bulletin of the Seismological Society of America*, 15(1), 1–72. <https://doi.org/10.1785/bssa0150020100>

Arnold, R., & Townend, J. (2007). A bayesian approach to estimating tectonic stress from seismological data. *Geophysical Journal International*, 170(3), 1336–1356. <https://doi.org/10.1111/j.1365-246X.2007.03485.x>

Bachmann, O., & Huber, C. (2016). Silicic magma reservoirs in the Earth's crust. *American Mineralogist*, 101(11), 2377–2404. <https://doi.org/10.2138/am-2016-5675>

Bain, A. A., Jellinek, A. M., & Wiebe, R. A. (2013). Quantitative field constraints on the dynamics of silicic magma chamber rejuvenation and overturn. *Contributions to Mineralogy and Petrology*, 165(6), 1275–1294. <https://doi.org/10.1007/s00410-013-0858-5>

Bannister, S., Sherburn, S., & Bourguignon, S. (2016). Earthquake swarm activity highlights crustal faulting associated with the Waimangu-Rotomahana-Mt Tarawera geothermal field, Taupo Volcanic Zone. *Journal of Volcanology and Geothermal Research*, 314, 49–56. <https://doi.org/10.1016/j.jvolgeores.2015.07.024>

Barberi, F., Corrado, G., Innocenti, F., & Luongo, G. (1984). Phlegraean fields 1982–1984: Brief chronicle of a volcano emergency in a densely populated area. *Bulletin Volcanologique*, 47(2), 175–185. <https://doi.org/10.1007/BF01961547>

Barker, S. J., Rowe, M. C., Wilson, C. J. N., Gamble, J. A., Rooyakkers, S. M., Wysoczanski, R. J., et al. (2020). What lies beneath? Reconstructing the primitive magmas fueling voluminous silicic volcanism using olivine-hosted melt inclusions. *Geology*, 48(5), 504–508. <https://doi.org/10.1130/G47422.1>

Barker, S. J., Van Eaton, A. R., Mastin, L. G., Wilson, C. J. N., Thompson, M. A., Wilson, T. M., et al. (2019). Modeling ash dispersal from future eruptions of Taupo supervolcano. *Geochemistry, Geophysics, Geosystems*, 20(7), 3375–3401. <https://doi.org/10.1029/2018GC008152>

Barker, S. J., Wilson, C. J. N., Allan, A. S. R., & Schipper, C. I. (2015). Fine-scale temporal recovery, reconstruction and evolution of a post-supereruption magmatic system. *Contributions to Mineralogy and Petrology*, 170(1), 5. <https://doi.org/10.1007/s00410-015-1155-2>

Barker, S. J., Wilson, C. J. N., Illsley-Kemp, F., Leonard, G. S., Mestel, E. R. H., Mauriohoo, K., & Charlier, B. L. A. (2021). Taupō: An overview of New Zealand's youngest supervolcano. *New Zealand Journal of Geology and Geophysics*, 64. <https://doi.org/10.1007/s00410-015-1155-2>

Barker, S. J., Wilson, C. J. N., Morgan, D. J., & Rowland, J. V. (2016). Rapid priming, accumulation, and recharge of magma driving recent eruptions at a hyperactive caldera volcano. *Geology*, 44(4), 323–326. <https://doi.org/10.1130/G37382.1>

Barker, S. J., Wilson, C. J. N., Smith, E. G. C., Charlier, B. L. A., Wooden, J. L., Hiess, J., & Ireland, T. R. (2014). Post-supereruption magmatic reconstruction of Taupo volcano (New Zealand), as reflected in zircon ages and trace elements. *Journal of Petrology*, 55(8), 1511–1533. <https://doi.org/10.1093/petrology/egu032>

Benson, T. W., Illsley-Kemp, F., Elms, H. C., Hamling, I. J., Savage, M. K., Wilson, C. J. N., et al. (2021). Earthquake analysis suggests dyke intrusion in 2019 near Tarawera volcano, New Zealand. *Frontiers in Earth Science*, 8, 606992. <https://doi.org/10.3389/feart.2020.606992>

Beyreuther, M., Barsch, R., Krischer, L., Megies, T., Behr, Y., & Wassermann, J. (2010). ObsPy: A Python toolbox for seismology. *Seismological Research Letters*, 81(3), 530–533. <https://doi.org/10.1785/gssrl.81.3.530>

Bibby, H. M., Caldwell, T. G., Davey, F. J., & Webb, T. H. (1995). Geophysical evidence on the structure of the Taupo Volcanic Zone and its hydrothermal circulation. *Journal of Volcanology and Geothermal Research*, 68(1–3), 29–58. [https://doi.org/10.1016/0377-0273\(95\)00007-H](https://doi.org/10.1016/0377-0273(95)00007-H)

Bryan, C. J., Sherburn, S., Bibby, H. M., Bannister, S. C., & Hurst, A. W. (1999). Shallow seismicity of the central Taupo Volcanic Zone, New Zealand: Its distribution and nature. *New Zealand Journal of Geology and Geophysics*, 42(4), 533–542. <https://doi.org/10.1080/00288306.1999.9514859>

Caricchi, L., Burlini, L., Ulmer, P., Gerya, T., Vassalli, M., & Papale, P. (2007). Non-Newtonian rheology of crystal-bearing magmas and implications for magma ascent dynamics. *Earth and Planetary Science Letters*, 264(3–4), 402–419. <https://doi.org/10.1016/j.epsl.2007.09.032>

Carrara, A., Burgisser, A., & Bergantz, G. W. (2020). The architecture of an intrusion in magmatic mush. *Earth and Planetary Science Letters*, 549, 116539. <https://doi.org/10.1016/j.epsl.2020.116539>

Chamberlain, C. J., Hopp, C. J., Boese, C. M., Warren-Smith, E., Chambers, D., Chu, S. X., et al. (2018). EQcorrscan: Repeating and near-repeating earthquake detection and analysis in python. *Seismological Research Letters*, 89(1), 173–181. <https://doi.org/10.1785/0220170151>

Chang, W.-L., Smith, R. B., Wicks, C., Farrell, J. M., & Puskas, C. M. (2007). Accelerated uplift and magmatic intrusion of the Yellowstone caldera, 2004 to 2006. *Science*, 318(5852), 952–956. <https://doi.org/10.1126/science.1146842>

Charlier, B. L. A., Wilson, C. J. N., & Mortimer, N. (2010). Evidence from zircon U-Pb age spectra for crustal structure and felsic magma genesis at Taupo volcano, New Zealand. *Geology*, 38(10), 915–918. <https://doi.org/10.1130/G31123.1>

Charlton, D., Kilburn, C., & Edwards, S. (2020). Volcanic unrest scenarios and impact assessment at Campi Flegrei caldera, Southern Italy. *Journal of Applied Volcanology*, 9(1), 7. <https://doi.org/10.1186/s13617-020-00097-x>

Chiarabba, C., & Moretti, M. (2006). An insight into the unrest phenomena at the Campi Flegrei caldera from Vp and Vp/Vs tomography. *Terra Nova*, 18(6), 373–379. <https://doi.org/10.1111/j.1365-3121.2006.00701.x>

Christiansen, R. L. (2001). *The Quaternary and Pliocene Yellowstone Plateau volcanic field of Wyoming, Idaho, and Montana (Vol. 729-G) (Nos. 1–143)*. United States Geological Survey Professional Papers. <https://doi.org/10.3133/pp729G>

- Christiansen, R. L., Lowenstern, J. B., Smith, R. B., Heasler, H., Morgan, L. A., Nathenson, M., et al. (2007). *Preliminary assessment of volcanic and hydrothermal hazards in Yellowstone National park and vicinity (United States Geological survey open-file report Nos. 2007-1071, 1–94)*. U. S. Geological Survey. <https://doi.org/10.3133/ofr20071071>
- Clarke, J., Adam, L., Sarout, J., van Wijk, K., Kennedy, B., & Dautriat, J. (2019). The relation between viscosity and acoustic emissions as a laboratory analogue for volcano seismicity. *Geology*, *47*(6), 499–503. <https://doi.org/10.1130/G45446.1>
- Cordonnier, B., Caricchi, L., Pistone, M., Castro, J., Hess, K.-U., Gottschaller, S., et al. (2012). The viscous-brittle transition of crystal-bearing silicic melt: Direct observation of magma rupture and healing. *Geology*, *40*(7), 611–614. <https://doi.org/10.1130/G3914.1>
- Cramer, F. (2021). *Scientific colour maps*. Zenodo. <https://doi.org/10.5281/zenodo.449129310.5281/zenodo.4491293>
- Davy, B. W., & Caldwell, T. G. (1998). Gravity, magnetic and seismic surveys of the caldera complex, Lake Taupo, North Island, New Zealand. *Journal of Volcanology and Geothermal Research*, *81*(1–2), 69–89. [https://doi.org/10.1016/S0377-0273\(97\)00074-7](https://doi.org/10.1016/S0377-0273(97)00074-7)
- de Ronde, C. E. J., Stoffers, P., Garbe-Schönberg, D., Christenson, B. W., Jones, B., Manconi, R., et al. (2002). Discovery of active hydrothermal venting in Lake Taupo, New Zealand. *Journal of Volcanology and Geothermal Research*, *115*(3–4), 257–275. [https://doi.org/10.1016/S0377-0273\(01\)00332-8](https://doi.org/10.1016/S0377-0273(01)00332-8)
- Dingwell, D. B. (1996). Volcanic dilemma—Flow or blow? *Science*, *273*(5278), 1054–1055. <https://doi.org/10.1126/science.273.5278.1054>
- Dunbar, N. W., Hervig, R. L., & Kyle, P. R. (1989). Determination of pre-eruptive H₂O, F and Cl contents of silicic magmas using melt inclusions: Examples from Taupo volcanic center, New Zealand. *Bulletin of Volcanology*, *51*(3), 177–184. <https://doi.org/10.1007/BF01067954>
- Dunbar, N. W., Iverson, N. A., Van Eaton, A. R., Sigl, M., Alloway, B. V., Kurbatov, A. V., et al. (2017). New Zealand supereruption provides time marker for the Last Glacial Maximum in Antarctica. *Scientific Reports*, *7*(1), 12238. <https://doi.org/10.1038/s41598-017-11758-0>
- Eberhart-Phillips, D., Bannister, S., & Reyners, M. (2020). Attenuation in the mantle wedge beneath super-volcanoes of the Taupo Volcanic Zone, New Zealand. *Geophysical Journal International*, *220*(1), 703–723. <https://doi.org/10.1093/gji/egz455>
- Eberhart-Phillips, D., Reyners, M., Bannister, S., Chadwick, M., & Ellis, S. (2010). Establishing a versatile 3-D seismic velocity model for New Zealand. *Seismological Research Letters*, *81*(6), 992–1000. <https://doi.org/10.1785/gssrl.81.6.992>
- Ebinger, C. J., Keir, D., Ayele, A., Calais, E., Wright, T. J., Belachew, M., et al. (2008). Capturing magma intrusion and faulting processes during continental rupture: Seismicity of the Dabbahu (Afar) rift. *Geophysical Journal International*, *174*(3), 1138–1152. <https://doi.org/10.1111/j.1365-246X.2008.03877.x>
- Ebinger, C. J., Oliva, S. J., Pham, T.-Q., Peterson, K., Chindandali, P., Illsley-Kemp, F., et al. (2019). Kinematics of active deformation in the Malawi Rift and Rungwe Volcanic Province, Africa. *Geochemistry, Geophysics, Geosystems*, *20*(8), 3928–3951. <https://doi.org/10.1029/2019GC008354>
- Ellis, S. M., Wilson, C. J. N., Bannister, S., Bibby, H. M., Heise, W., Wallace, L., & Patterson, N. (2007). A future magma inflation event under the rhyolitic Taupo volcano, New Zealand: Numerical models based on constraints from geochemical, geological, and geophysical data. *Journal of Volcanology and Geothermal Research*, *168*, 1–27. <https://doi.org/10.1016/j.jvolgeores.2007.06.004>
- Froggatt, P. C. (1981). Stratigraphy and nature of Taupo Pumice Formation. *New Zealand Journal of Geology and Geophysics*, *24*(2), 231–248. <https://doi.org/10.1080/00288306.1981.10422715>
- Goitom, B., Oppenheimer, C., Hammond, J. O. S., Grandin, R., Barnie, T., Donovan, A., et al. (2015). First recorded eruption of Nabro volcano, Eritrea, 2011. *Bulletin of Volcanology*, *77*(10), 85. <https://doi.org/10.1007/s00445-015-0966-3>
- Greenfield, T., Keir, D., Kendall, J.-M., & Ayele, A. (2019). Seismicity of the Bora-Tullu Moye volcanic field, 2016–2017. *Geochemistry, Geophysics, Geosystems*, *20*(2), 548–570. <https://doi.org/10.1029/2018GC007648>
- Gualda, G. A. R., Ghiorsio, M. S., Lemons, R. V., & Carley, T. L. (2012). Rhyolite-MELTS: A modified calibration of MELTS optimized for silica-rich, fluid-bearing magmatic systems. *Journal of Petrology*, *53*(5), 875–890. <https://doi.org/10.1093/ptrology/egr080>
- Harrison, A., & White, R. S. (2006). Lithospheric structure of an active backarc basin: The Taupo Volcanic Zone, New Zealand. *Geophysical Journal International*, *167*(2), 968–990. <https://doi.org/10.1111/j.1365-246X.2006.03166.x>
- Hayes, G., Reyners, M., & Stuart, G. (2004). The Waiouru, New Zealand, earthquake swarm: Persistent mid crustal activity near an active volcano. *Geophysical Research Letters*, *31*(19), L19613. <https://doi.org/10.1029/2004GL020709>
- Healy, J. (1964). Stratigraphy and chronology of late quaternary volcanic ash in Taupo, Rotorua and Gisborne districts. Part 1. Dating of the younger volcanic eruptions of the Taupo region. *New Zealand Geological Survey Bulletin*, *73*, 7–42.
- Heimann, S., Kriegerowski, M., Isken, M., Cesca, S., Daout, S., Grigoli, F., et al. (2017). *Pyrocko-An open-source seismology toolbox and library*. GFZ Data Services. <https://doi.org/10.5880/GFZ.2.1.2017.001>
- Herring, T. A., King, R. W., & McClusky, S. C. (2010). *Introduction to gamit/globk [Computer software manual]* (71 ed., p. 10). Cambridge, MA: Citeseer.
- Hess, K. U., & Dingwell, D. B. (1996). Viscosities of hydrous leucogranitic melts: A non-Arrhenian model. *American Mineralogist: Journal of Earth and Planetary Materials*, *81*(9–10), 1297–1300.
- Hildreth, W. (2017). Fluid-driven uplift at Long Valley Caldera, California: Geologic perspectives. *Journal of Volcanology and Geothermal Research*, *341*, 269–286. <https://doi.org/10.1016/j.jvolgeores.2017.06.010>
- Hill, D. P. (2006). *Unrest in Long Valley caldera, California, 1978–2004* (Vol. 269, pp. 1–24). Geological Society, London, Special Publications. <https://doi.org/10.1144/GSL.SP.2006.269.01.02>
- Hill, D. P., Dawson, P., Johnston, M. J. S., Pitt, A. M., Biasi, G., & Smith, K. (2002). Very-long-period volcanic earthquakes beneath Mammoth Mountain, California. *Geophysical Research Letters*, *29*(10), 1370–1371. <https://doi.org/10.1029/2002GL014833>
- Hill, D. P., Montgomery-Brown, E., Shelly, D. R., Flinders, A., & Prejean, S. (2020). Post-1978 tumescence at Long Valley Caldera, California: A geophysical perspective. *Journal of Volcanology and Geothermal Research*, *400*, 106900. <https://doi.org/10.1016/j.jvolgeores.2020.106900>
- Hincks, T. K., Komorowski, J.-C., Sparks, S. R., & Aspinall, W. P. (2014). Retrospective analysis of uncertain eruption precursors at La Soufrière volcano, Guadeloupe, 1975–77: Volcanic hazard assessment using a Bayesian Belief Network approach. *Journal of Applied Volcanology*, *3*(1), 3. <https://doi.org/10.1186/2191-5040-3-3>
- Hogg, A. G., Lowe, D. J., Palmer, J., Boswijk, G., & Ramsey, C. B. (2012). Revised calendar date for the Taupo eruption derived by ¹⁴C wiggle-matching using a New Zealand kauri ¹⁴C calibration data set. *The Holocene*, *22*(4), 439–449. <https://doi.org/10.1177/0959683611425551>
- Hogg, A. G., Wilson, C. J. N., Lowe, D. J., Turney, C. S. M., White, P., Lorrey, A. M., et al. (2019). Wiggle-match radiocarbon dating of the Taupo eruption. *Nature Communications*, *10*(1), 4669. <https://doi.org/10.1038/s41467-019-12532-8>
- Hotovec-Ellis, A. J., Shelly, D. R., Hill, D. P., Pitt, A. M., Dawson, P. B., & Chouet, B. A. (2018). Deep fluid pathways beneath Mammoth Mountain, California, illuminated by migrating earthquake swarms. *Science Advances*, *4*(8), eaat5258. <https://doi.org/10.1126/sciadv.aat5258>
- Houghton, B. F., Carey, R. J., Cashman, K. V., Wilson, C. J. N., Hobden, B. J., & Hammer, J. E. (2010). Diverse patterns of ascent, degassing, and eruption of rhyolite magma during the 1.8 ka Taupo eruption, New Zealand: Evidence from clast vesicularity. *Journal of Volcanology and Geothermal Research*, *195*(1), 31–47. <https://doi.org/10.1016/j.jvolgeores.2010.06.002>

- Houghton, B. F., Carey, R. J., & Rosenberg, M. D. (2014). The 1800a Taupo eruption: "Ill wind" blows the ultraplinian type event down to Plinian. *Geology*, 42(5), 459–461. <https://doi.org/10.1130/G35400.1>
- Hughes, G. R., & Mahood, G. A. (2011). Silicic calderas in arc settings: Characteristics, distribution, and tectonic controls. *GSA Bulletin*, 123(7–8), 1577–1595. <https://doi.org/10.1130/B30232.1>
- Hunter, J. D. (2007). Matplotlib: A 2D graphics environment. *Computing in Science & Engineering*, 9(3), 90–95. <https://doi.org/10.1109/MCSE.2007.55>
- Husen, S., Taylor, R., Smith, R. B., & Healsler, H. (2004). Changes in geyser eruption behavior and remotely triggered seismicity in Yellowstone National Park produced by the 2002 M 7.9 Denali fault earthquake, Alaska. *Geology*, 32(6), 537–540. <https://doi.org/10.1130/G20381.1>
- Hutchison, W., Biggs, J., Mather, T. A., Pyle, D. M., Lewi, E., Yirgu, G., et al. (2016). Causes of unrest at silicic calderas in the East African Rift: New constraints from InSAR and soil-gas chemistry at Aluto volcano, Ethiopia. *Geochemistry, Geophysics, Geosystems*, 17(8), 3008–3030. <https://doi.org/10.1002/2016GC006395>
- Hutton, L., & Boore, D. M. (1987). The M_L scale in southern California. *Bulletin of the Seismological Society of America*, 77(6), 2074–2094.
- Illsley-Kemp, F., Barker, S. J., Smith, B., & Wilson, C. J. N. (2020). Implications of a supervolcano's seismicity. *EOS, Transactions of the American Geophysical Union*, 101(6), 28–32. <https://doi.org/10.1029/2020EO140955>
- Illsley-Kemp, F., Keir, D., Bull, J. M., Ayele, A., Hammond, J. O., Kendall, J.-M., et al. (2017). Local earthquake magnitude scale and b-value for the Danakil region of northern Afar. *Bulletin of the Seismological Society of America*, 107(2), 521–531. <https://doi.org/10.1785/0120150253>
- Illsley-Kemp, F., Savage, M. K., Wilson, C. J. N., & Bannister, S. (2019). Mapping stress and structure from subducting slab to magmatic rift: Crustal seismic anisotropy of the North Island, New Zealand. *Geochemistry, Geophysics, Geosystems*, 20(11), 5038–5056. <https://doi.org/10.1029/2019GC008529>
- Janiszewski, H. A., Wagner, L. S., & Roman, D. C. (2020). Aseismic mid-crustal magma reservoir at Cleveland Volcano imaged through novel receiver function analyses. *Scientific Reports*, 10(1), 1–9. <https://doi.org/10.1038/s41598-020-58589-0>
- Johnston, D., Scott, B., Houghton, B., Paton, D., Dowrick, D., Villamor, P., & Savage, J. (2002). Social and economic consequences of historic caldera unrest at the Taupo volcano, New Zealand and the management of future episodes of unrest. *Bulletin of the New Zealand Society of Earthquake Engineering*, 35(4), 215–230. <https://doi.org/10.5459/bnzsee.35.4.215-230>
- Keir, D., Stuart, G., Jackson, A., & Ayele, A. (2006). Local earthquake magnitude scale and seismicity rate for the Ethiopian Rift. *Bulletin of the Seismological Society of America*, 96(6), 2221–2230. <https://doi.org/10.1785/0120060051>
- Lamarque, G., Barnes, P. M., & Bull, J. M. (2006). Faulting and extension rate over the last 20,000 years in the offshore Whakatane Graben, New Zealand continental shelf. *Tectonics*, 25(4), TC4005. <https://doi.org/10.1029/2005TC001886>
- Langridge, R. M., Ries, W. F., Litchfield, N. J., Villamor, P., Van Dissen, R. J., Barrell, D. J. A., et al. (2016). The New Zealand active faults database. *New Zealand Journal of Geology and Geophysics*, 59(1), 86–96. <https://doi.org/10.1080/00288306.2015.1112818>
- Lavayssière, A., Drooff, C., Ebinger, C., Gallacher, R., Illsley-Kemp, F., Oliva, S. J., & Keir, D. (2019). Depth extent and kinematics of faulting in the southern Tanganyika rift, Africa. *Tectonics*, 38(3), 842–862. <https://doi.org/10.1029/2018TC005379>
- Lavayssière, A., Greenfield, T., Keir, D., Ayele, A., & Kendall, J.-M. (2019). Local seismicity near the actively deforming Corbetti volcano in the Main Ethiopian Rift. *Journal of Volcanology and Geothermal Research*, 381, 227–237. <https://doi.org/10.1016/j.jvolgeores.2019.06.008>
- Lavigne, F., Degeai, J.-P., Komorowski, J.-C., Guillet, S., Robert, V., Lahitte, P., et al. (2013). Source of the great AD 1257 mystery eruption unveiled, Samalas volcano, Rinjani Volcanic complex, Indonesia. *Proceedings of the National Academy of Sciences*, 110(42), 16742–16747. <https://doi.org/10.1073/pnas.1307520110>
- Lomax, A., Virieux, J., Volant, P., & Berge-Thierry, C. (2000). Probabilistic earthquake location in 3D and layered models. *Modern Approaches in Geophysics*, 18, 101–134. https://doi.org/10.1007/978-94-015-9536-0_5
- Longo, M. L. (2019). How memory can reduce the vulnerability to disasters: The bradyseism of Pozzuoli in southern Italy. *AIMS Geosciences*, 5(3), 631–644. <https://doi.org/10.3934/geosci.2019.3.631>
- Lowenstern, J. B., Smith, R. B., & Hill, D. P. (2006). Monitoring super-volcanoes: Geophysical and geochemical signals at Yellowstone and other large caldera systems. *Philosophical Transactions of the Royal Society A: Mathematical, Physical & Engineering Sciences*, 364(1845), 2055–2072. <https://doi.org/10.1098/rsta.2006.1813>
- Lyard, F., Lefevre, F., Letellier, T., & Francis, O. (2006). Modelling the global ocean tides: Modern insights from FES2004. *Ocean Dynamics*, 56(5–6), 394–415. <https://doi.org/10.1007/s10236-006-0086-x>
- Magee, C., Stevenson, C. T. E., Ebmeier, S. K., Keir, D., Hammond, J. O. S., Gottsmann, J. H., et al. (2018). Magma plumbing systems: A geophysical perspective. *Journal of Petrology*, 59(6), 1217–1251. <https://doi.org/10.1093/ptrology/egy064>
- Maj, M., Starace, F., Crepet, P., Lobracc, S., Veltro, F., De Marco, F., & Kemali, D. (1989). Prevalence of psychiatric disorders among subjects exposed to a natural disaster. *Acta Psychiatrica Scandinavica*, 79(6), 544–549. <https://doi.org/10.1111/j.1600-0447.1989.tb10301.x>
- Maron, S. H., & Pierce, P. E. (1956). Application of Ree-Eyring generalized flow theory to suspensions of spherical particles. *Journal of Colloid Science*, 11(1), 80–95. [https://doi.org/10.1016/0095-8522\(56\)90023-x](https://doi.org/10.1016/0095-8522(56)90023-x)
- Mason, B. G., Pyle, D. M., & Oppenheimer, C. (2004). The size and frequency of the largest explosive eruptions on earth. *Bulletin of Volcanology*, 66(8), 735–748. <https://doi.org/10.1007/s00445-004-0355-9>
- Mei, E. T. W., Lavigne, F., Picquout, A., De Bézilal, E., Brunstein, D., Grancher, D., et al. (2013). Lessons learned from the 2010 evacuations at Merapi volcano. *Journal of Volcanology and Geothermal Research*, 261, 348–365. <https://doi.org/10.1016/j.jvolgeores.2013.03.010>
- Mogi, K. (1958). Relations between the eruptions of various volcanoes and the deformations of the ground surfaces around them. *Bulletin of the Earthquake Research Institute*, 36, 99–134.
- Mueller, S., Llewellyn, E. W., & Mader, H. M. (2010). The rheology of suspensions of solid particles. *Proceedings of the Royal Society A: Mathematical, Physical & Engineering Sciences*, 466(2116), 1201–1228. <https://doi.org/10.1098/rspa.2009.0445>
- Muirhead, J. D., Wright, L. J. M., & Scholz, C. A. (2019). Rift evolution in regions of low magma input in East Africa. *Earth and Planetary Science Letters*, 506, 332–346. <https://doi.org/10.1016/j.epsl.2018.11.004>
- Myers, M. L., Wallace, P. J., & Wilson, C. J. N. (2019). Inferring magma ascent timescales and reconstructing conduit processes in explosive rhyolitic eruptions using diffusive losses of hydrogen from melt inclusions. *Journal of Volcanology and Geothermal Research*, 369, 95–112. <https://doi.org/10.1016/j.jvolgeores.2018.11.009>
- Myers, M. L., Wallace, P. J., Wilson, C. J. N., Watkins, J. M., & Liu, Y. (2018). Ascent rates of rhyolitic magma at the onset of three caldera-forming eruptions. *American Mineralogist*, 103(6), 952–965. <https://doi.org/10.2138/am-2018-6225>
- Nairn, I. A. (2002). *Geology of the Okataina volcanic center, scale 1:50,000 (Institute of Geological and Nuclear Sciences geological map No. 25)*. New Zealand: Lower Hutt Institute of Geological and Nuclear Sciences.

- Newhall, C. G., & Dzuris, D. (1988). *Historical unrest at the large calderas of the world*. (Vol. 2, 1855, pp. 1–1108). US Geological Survey Bulletin. <https://doi.org/10.3133/b1855>
- Otway, P. M. (1986). *Vertical deformation associated with the Taupo earthquake Swarm*. (Vol. 24, pp. 187–200). Royal Society of New Zealand Bulletin.
- Otway, P. M. (1987). Taupo Volcanic centre deformation surveys. *New Zealand Volcanological Record*, 15, 68–70.
- Otway, P. M. (1989). Vertical deformation monitoring by periodic water level observations, Lake Taupo, New Zealand. In J. H. Latter (Ed.), *Volcanic hazards* (Vol. 1, pp. 561–574). Berlin: Springer. https://doi.org/10.1007/978-3-642-73759-6_33
- Otway, P. M., Blick, G. H., & Scott, B. J. (2002). Vertical deformation at Lake Taupo, New Zealand, from lake levelling surveys, 1979–99. *New Zealand Journal of Geology and Geophysics*, 45(1), 121–132. <https://doi.org/10.1080/00288306.2002.9514964>
- Papale, P. (2018). Global time-size distribution of volcanic eruptions on Earth. *Scientific Reports*, 8(1), 6838. <https://doi.org/10.1038/s41598-018-25286-y>
- Petersen, T., Gledhill, K., Chadwick, M., Gale, N. H., & Ristau, J. (2011). The New Zealand national seismograph network. *Seismological Research Letters*, 82(1), 9–20. <https://doi.org/10.1785/gssrl.82.1.9>
- Peterson, D. E., Garibaldi, N., Keranen, K., Tikoff, B., Miller, C., Lara, L. E., et al. (2020). Active normal faulting, diking, and doming above the rapidly inflating Laguna del Maule Volcanic Field, Chile, imaged with CHIRP, magnetic, and focal mechanism data. *Journal of Geophysical Research: Solid Earth*, 125(8), e2019JB019329. <https://doi.org/10.1029/2019JB019329>
- Petford, N., & Koenders, M. A. (2003). Shear-induced pressure changes and seepage phenomena in a deforming porous layer-I. *Geophysical Journal International*, 155(3), 857–869. <https://doi.org/10.1111/j.1365-246X.2003.02076.x>
- Phillipson, G., Sobradelo, R., & Gottsmann, J. (2013). Global volcanic unrest in the 21st century: An analysis of the first decade. *Journal of Volcanology and Geothermal Research*, 264, 183–196. <https://doi.org/10.1016/j.jvolgeores.2013.08.004>
- Potter, S. H., Jolly, G. E., Neall, V. E., Johnston, D. M., & Scott, B. J. (2014). Communicating the status of volcanic activity: Revising New Zealand's volcanic alert level system. *Journal of Applied Volcanology*, 3(1), 13. <https://doi.org/10.1186/s13617-014-0013-7>
- Potter, S. H., Scott, B. J., Jolly, G. E., Johnston, D. M., & Neall, V. E. (2015). A catalogue of caldera unrest at Taupo Volcanic Centre, New Zealand, using the Volcanic Unrest Index (VUI). *Bulletin of Volcanology*, 77(9), 78. <https://doi.org/10.1007/s00445-015-0956-5>
- Potter, S. H., Scott, B. J., Jolly, G. E., Neall, V. E., & Johnston, D. M. (2015). Introducing the Volcanic Unrest Index (VUI): A tool to quantify and communicate the intensity of volcanic unrest. *Bulletin of Volcanology*, 77(9), 77. <https://doi.org/10.1007/s00445-015-0957-4>
- Pugh, D. J., & White, R. S. (2018). MTfit: A Bayesian approach to seismic moment tensor inversion. *Seismological Research Letters*, 89(4), 1507–1513. <https://doi.org/10.1785/0220170273>
- Reyners, M., Eberhart-Phillips, D., & Stuart, G. (2007). The role of fluids in lower-crustal earthquakes near continental rifts. *Nature*, 446(7139), 1075–1078. <https://doi.org/10.1038/nature05743>
- Richter, C. (1935). An instrumental earthquake magnitude scale. *Bulletin of the Seismological Society of America*, 25(1), 1–32. <https://doi.org/10.1785/bssa0250010001>
- RNZ. (2019). *Taupō cleanup begins after 190,000 litre sewage spill*. Retrieved from <https://www.rnz.co.nz/news/national/393516/taupo-cleanup-begins-after-190-000-litre-sewage-spill>
- Robock, A. (2000). Volcanic eruptions and climate. *Reviews of Geophysics*, 38(2), 191–219. <https://doi.org/10.1029/1998RG000054>
- Rose, W. L., & Chesner, C. A. (1987). Dispersal of ash in the great Toba eruption, 75 ka. *Geology*, 15(10), 913–917. [https://doi.org/10.1130/0091-7613\(1987\)15<913:doaitg>2.0.co;2](https://doi.org/10.1130/0091-7613(1987)15<913:doaitg>2.0.co;2)
- Rowe, C. D., Meneghini, F., & Moore, J. C. (2011). Textural record of the seismic cycle: Strain-rate variation in an ancient subduction thrust. *Geological Society, London, Special Publications*, 359(1), 77–95. <https://doi.org/10.1144/SP359.5>
- Rowland, J. V., & Sibson, R. H. (2001). Extensional fault kinematics within the Taupo Volcanic Zone, New Zealand: Soft-linked segmentation of a continental rift system. *New Zealand Journal of Geology and Geophysics*, 44(2), 271–283. <https://doi.org/10.1080/00288306.2001.9514938>
- Rowland, J. V., Wilson, C. J. N., & Gravelly, D. M. (2010). Spatial and temporal variations in magma-assisted rifting, Taupo Volcanic Zone, New Zealand. *Journal of Volcanology and Geothermal Research*, 190(1–2), 89–108. <https://doi.org/10.1016/j.jvolgeores.2009.05.004>
- Sandri, L., Acocella, V., & Newhall, C. (2017). Searching for patterns in caldera unrest. *Geochemistry, Geophysics, Geosystems*, 18(7), 2748–2768. <https://doi.org/10.1002/2017GC006870>
- Sandri, L., Marzocchi, W., & Zaccarelli, L. (2004). A new perspective in identifying the precursory patterns of eruptions. *Bulletin of Volcanology*, 66(3), 263–275. <https://doi.org/10.1007/s00445-003-0309-7>
- Schaer, S. (1999). *Mapping and predicting the Earth's ionosphere using the global positioning system* (Vol. 59). Institut für Geodäsie und Photogrammetrie, Eidgenössische Technische Hochschule.
- Schofield, N. J., Brown, D. J., Magee, C., & Stevenson, C. T. (2012). Sill morphology and comparison of brittle and non-brittle emplacement mechanisms. *Journal of the Geological Society*, 169, 127–141. <https://doi.org/10.1144/0016-76492011-078>
- Self, S. (2006). The effects and consequences of very large explosive volcanic eruptions. *Philosophical Transactions of the Royal Society A: Mathematical, Physical & Engineering Sciences*, 364(1845), 2073–2097. <https://doi.org/10.1098/rsta.2006.1814>
- Severne, C. M., & Hochstein, M. P. (1994). Heat and mass transfer of the Hipaua thermal area (Tokaanu-Waihi geothermal field) Lake Taupo, New Zealand. *Proceedings of the 16th New Zealand Geothermal Workshop* (pp. 209–214). University of Auckland.
- Shelly, D. R., Taira, T., Prejean, S. G., Hill, D. P., & Dreger, D. S. (2015). Fluid-faulting interactions: Fracture-mesh and fault-valve behavior in the February 2014 Mammoth Mountain, California, earthquake swarm. *Geophysical Research Letters*, 42(14), 5803–5812. <https://doi.org/10.1002/2015GL064325>
- Singer, B. S., Andersen, N. L., Le Mével, H., Feigl, K. L., DeMets, C., Tikoff, B., et al. (2014). Dynamics of a large, restless, rhyolitic magma system at Laguna del Maule, southern Andes, Chile. *Geological Society of America Today*, 24(12), 4–10. <https://doi.org/10.1130/gsatg216a.1>
- Smith, R. T. (1998). *Eruptive and depositional models for units 3 and 4 of the 1.85 ka Taupo eruption: Implications for the nature of large-scale wet eruptions* (Unpublished doctoral dissertation). Christchurch: University of Canterbury
- Smith, R. T., & Houghton, B. F. (1995). Vent migration and changing eruptive style during the 1800a Taupo eruption: New evidence from the Hatepe and Rotongaio phreatoplinian ashes. *Bulletin of Volcanology*, 57(6), 432–439. <https://doi.org/10.1007/BF00300987>
- Sparks, R. S. J. (2003). Forecasting volcanic eruptions. *Earth and Planetary Science Letters*, 210(1–2), 1–15. [https://doi.org/10.1016/S0012-821X\(03\)00124-9](https://doi.org/10.1016/S0012-821X(03)00124-9)
- Stagpoole, V., Miller, C., Caratori Tontini, F., Brakenrig, T., & Macdonald, N. (2020). A two million-year history of rifting and caldera volcanism imprinted in new gravity anomaly compilation of the Taupō Volcanic Zone, New Zealand. *New Zealand Journal of Geology and Geophysics*, 64, 1–14. <https://doi.org/10.1080/00288306.2020.1848882>

- Stern, T., & Benson, A. (2011). Wide-angle seismic imaging beneath an andesitic arc: Central North Island, New Zealand. *Journal of Geophysical Research*, 116, B09308. <https://doi.org/10.1029/2011JB008337>
- Stern, T., Stratford, W., Seward, A., Henderson, M., Savage, M., Smith, E., et al. (2010). Crust-mantle structure of the central North Island, New Zealand, based on seismological observations. *Journal of Volcanology and Geothermal Research*, 190(1–2), 58–74. <https://doi.org/10.1016/j.jvolgeores.2009.11.017>
- Stratford, W. R., & Stern, T. A. (2006). Crust and upper mantle structure of a continental backarc: Central North Island, New Zealand. *Geophysical Journal International*, 166(1), 469–484. <https://doi.org/10.1111/j.1365-246X.2006.02967.x>
- Sutton, A. N., Blake, S., Wilson, C. J. N., & Charlier, B. L. A. (2000). Late Quaternary evolution of a hyperactive rhyolite magmatic system: Taupo volcanic centre, New Zealand. *Journal of the Geological Society*, 157, 537–552. <https://doi.org/10.1144/jgs.157.3.537>
- Syahbana, D. K., Kasbani, K., Suantika, G., Prambada, O., Andreas, A., Saing, U., et al. (2019). The 2017–19 activity at Mount Agung in Bali (Indonesia): Intense unrest, monitoring, crisis response, evacuation, and eruption. *Scientific Reports*, 9(1), 8848. <https://doi.org/10.1038/s41598-019-45295-9>
- Takarada, S., & Hoshizumi, H. (2020). Distribution and eruptive volume of Aso-4 pyroclastic density current and tephra fall deposits, Japan: An M8 super-eruption. *Frontiers in Earth Science*, 8, 170. <https://doi.org/10.3389/feart.2020.00170>
- Tizzani, P., Battaglia, M., Zeni, G., Atzori, S., Berardino, P., & Lanari, R. (2009). Uplift and magma intrusion at Long Valley caldera from InSAR and gravity measurements. *Geology*, 37(1), 63–66. <https://doi.org/10.1130/G25318A.1>
- Townend, J., Sherburn, S., Arnold, R., Boese, C., & Woods, L. (2012). Three-dimensional variations in present-day tectonic stress along the Australia-Pacific plate boundary in New Zealand. *Earth and Planetary Science Letters*, 353–354, 47–59. <https://doi.org/10.1016/j.epsl.2012.08.003>
- Troise, C., De Natale, G., Pingue, F., Obrizzo, F., De Martino, P., Tammara, U., & Boschi, E. (2007). Renewed ground uplift at Campi Flegrei caldera (Italy): New insight on magmatic processes and forecast. *Geophysical Research Letters*, 34(3), L03301. <https://doi.org/10.1029/2006GL028545>
- Troise, C., De Natale, G., Schiavone, R., Somma, R., & Moretti, R. (2019). The Campi Flegrei caldera unrest: Discriminating magma intrusions from hydrothermal effects and implications for possible evolution. *Earth-Science Reviews*, 188, 108–122. <https://doi.org/10.1016/j.earscirev.2018.11.007>
- Trugman, D. T., & Shearer, P. M. (2017). GrowClust: A hierarchical clustering algorithm for relative earthquake relocation, with application to the Spanish Springs and Sheldon, Nevada, earthquake sequences. *Seismological Research Letters*, 88(2A), 379–391. <https://doi.org/10.1785/0220160188>
- Uchide, T., Horikawa, H., Nakai, M., Matsushita, R., Shigematsu, N., Ando, R., & Imanishi, K. (2016). The 2016 Kumamoto-Oita earthquake sequence: Aftershock seismicity gap and dynamic triggering in volcanic areas. *Earth Planets and Space*, 68(1), 180. <https://doi.org/10.1186/s40623-016-0556-4>
- Utsu, T., Ogata, Y., & Matsu'ura, R. S. (1995). The centenary of the Omori formula for a decay law of aftershock activity. *Journal of Physics of the Earth*, 43(1), 1–33. <https://doi.org/10.4294/jpe1952.43.1>
- Villamor, P., Berryman, K. R., Ellis, S. M., Schreurs, G., Wallace, L. M., Leonard, G. S., et al. (2017). Rapid evolution of subduction-related continental intraarc rifts: The Taupo Rift, New Zealand. *Tectonics*, 36(10), 2250–2272. <https://doi.org/10.1002/2017TC004715>
- Von Lichten, I. J., White, J. D. L., Manville, V., & Ohneiser, C. (2016). Giant rafted pumice blocks from the most recent eruption of Taupo volcano, New Zealand: Insights from palaeomagnetic and textural data. *Journal of Volcanology and Geothermal Research*, 318, 73–88. <https://doi.org/10.1016/j.jvolgeores.2016.04.003>
- Wadsworth, F. B., Witcher, T., Vossen, C. E. J., Hess, K.-U., Unwin, H. E., Scheu, B., et al. (2018). Combined effusive-explosive silicic volcanism straddles the multiphase viscous-to-brittle transition. *Nature Communications*, 9(1), 4696. <https://doi.org/10.1038/s41467-018-07187-w>
- Wallace, L. M., Beavan, J., McCaffrey, R., & Darby, D. (2004). Subduction zone coupling and tectonic block rotations in the North Island, New Zealand. *Journal of Geophysical Research: Solid Earth*, 109(12), B12406. <https://doi.org/10.1029/2004JB003241>
- Warren-Smith, E., Chamberlain, C. J., Lamb, S., & Townend, J. (2017). High-precision analysis of an aftershock sequence using matched-filter detection: The 4 May 2015 M_L 6 Wanaka earthquake, Southern Alps, New Zealand. *Seismological Research Letters*, 88(4), 1065–1077. <https://doi.org/10.1785/0220170016>
- Wessel, P., Luis, J. F., Uieda, L., Scharroo, R., Wobbe, F., Smith, W. H. F., & Tian, D. (2019). The generic mapping tools version 6. *Geochemistry, Geophysics, Geosystems*, 20(11), 5556–5564. <https://doi.org/10.1029/2019GC008515>
- Whiteford, P. C. (1996). Heat flow in the sediments of Lake Taupo, New Zealand. *Tectonophysics*, 257(1), 81–92. [https://doi.org/10.1016/0040-1951\(95\)00122-0](https://doi.org/10.1016/0040-1951(95)00122-0)
- Wiemer, S., & Wyss, M. (2000). Minimum magnitude of completeness in earthquake catalogs: Examples from Alaska, the western United States, and Japan. *Bulletin of the Seismological Society of America*, 90(4), 859–869. <https://doi.org/10.1785/0119990114>
- Wilson, C. J. N. (1985). The Taupo eruption, New Zealand. II. The Taupo ignimbrite. *Philosophical Transactions of the Royal Society A: Mathematical, Physical & Engineering Sciences*, 314(1529), 229–310. <https://doi.org/10.1098/rsta.1985.0020>
- Wilson, C. J. N. (1993). Stratigraphy, chronology, styles and dynamics of late Quaternary eruptions from Taupo volcano, New Zealand. *Philosophical Transactions of the Royal Society A: Mathematical, Physical & Engineering Sciences*, 343(1668), 205–306. <https://doi.org/10.1098/rsta.1993.0050>
- Wilson, C. J. N. (2001). The 26.5 ka Oruanui eruption, New Zealand: An introduction and overview. *Journal of Volcanology and Geothermal Research*, 112(1–4), 133–174. [https://doi.org/10.1016/S0377-0273\(01\)00239-6](https://doi.org/10.1016/S0377-0273(01)00239-6)
- Wilson, C. J. N. (2017). Volcanoes: Characteristics, tipping points, and those pesky unknown unknowns. *Elements*, 13(1), 41–46. <https://doi.org/10.2113/gselements.13.1.41>
- Wilson, C. J. N., Gravley, D. M., Leonard, G. S., & Rowland, J. V. (2009). Volcanism in the central Taupo Volcanic Zone, New Zealand: Tempo, styles and controls. In *Studies in volcanology: The legacy of George Walker* (Vol. 2, pp. 225–247). Special Publications of IAVCEI. <https://doi.org/10.1144/iavgl002.12>
- Wilson, C. J. N., Houghton, B. F., McWilliams, M. O., Lanphere, M. A., Weaver, S. D., & Briggs, R. M. (1995). Volcanic and structural evolution of Taupo Volcanic Zone, New Zealand: A review. *Journal of Volcanology and Geothermal Research*, 68(1–3), 1–28. [https://doi.org/10.1016/0377-0273\(95\)00006-G](https://doi.org/10.1016/0377-0273(95)00006-G)
- Wilson, C. J. N., & Walker, G. P. L. (1985). The Taupo eruption, New Zealand I. General aspects. *Philosophical Transactions of the Royal Society A: Mathematical, Physical & Engineering Sciences*, 314(1529), 199–228. <https://doi.org/10.1098/rsta.1985.0019>
- Wright, T. L., & Klein, F. W. (2006). Deep magma transport at Kilauea volcano, Hawaii. *Lithos*, 87(1–2), 50–79. <https://doi.org/10.1016/j.lithos.2005.05.004>